Bi$_2$O$_3$ boosts Brightness, Biocompatibility and Stability of Mn-doped Ba$_3$(VO$_4$)$_2$ as NIR-II Contrast Agent

Supporting Information

Pascal M. Gschwend[1], Kerda Keevend[2,3], Marianne Aellen[4], Alexander Gogos[2], Frank Krumeich[5], Inge K. Herrmann[2,3], Sotiris E. Pratsinis[1]*

[1] Particle Technology Laboratory, Institute of Process Engineering, Department of Mechanical and Process Engineering, ETH Zürich, Sonneggstrasse 3, CH-8092 Zurich, Switzerland

[2] Particles-Biology Interactions, Department Materials Meet Life, Swiss Federal Laboratories for Materials Science and Technology (Empa), Lerchenfeldstrasse 5, CH-9014 St. Gallen, Switzerland

[3] Nanoparticle Systems Engineering Laboratory, Institute of Process Engineering, Department of Mechanical and Process Engineering, ETH Zürich, Sonneggstrasse 3, CH-8092 Zurich, Switzerland

[4] Optical Materials Engineering Laboratory, Institute of Process Engineering, Department of Mechanical and Process Engineering, ETH Zürich, Leonhardstrasse 21, CH-8092 Zurich, Switzerland

[5] Laboratory for Inorganic Chemistry, Department of Chemistry and Applied Biosciences, ETH Zürich, Vladimir-Prelog-Weg 1, CH-8093 Zurich, Switzerland

* Corresponding author: pratsinis@ethz.ch

SI-I: Optimization and characterization of $Ba_3(VO_4)_2$:Mn^{5+} nanoparticles

Figure S1a shows the XRD patterns of as-prepared and annealed particles (doped with 0.5 % Mn^{5+}) from 400 to 800 °C for 2h in air. The as-prepared nanoparticles consist primarily of rhombohedral $Ba_3(VO_4)_2$ (squares). Additional peaks, possibly originating from other phases with the Ba-V-O system (e.g., $Ba_4V_2O_9$, $BaVO_3$, BaV_3O_8), become less apparent and eventually disappear with increasing annealing temperature.

This thermal treatment increases primary particle (Figure S1b, d_{BET}, circles) and crystal sizes (d_{XRD}, triangles) and alters particle morphology (Figure S1b, insets). As-prepared particles are spherical (Figure S1c) having a log-normal size distribution with a geometric mean and standard deviation of 24 nm and 1.48, respectively (Figure S2a). The d_{BET} of as-prepared particles (31 nm) is comparable to that observed in microscopy (Fig. S2a).

After annealing at 600 °C, aggregated (sinter-bonded) particles are observed (Figure S1d) that were formed by sintering or coalescence of single particles. Their geometric mean of the shortest and longest axes are 40 and 47 nm (Figure S2b). The crystal and primary particle sizes remain in good agreement up to 600 °C. However, at 700 °C the primary particle size drastically increases up to 270 nm while the crystal size is 75 nm, indicating polycrystalline particles. Their microscopy size was 61 and 77 nm for the short and long axis, respectively (Figure S1e and S2c). At 800 °C strongly aggregated particles were formed that could not be dispersed in water and had too low specific surface area to be measured reliably.Nanoparticles post-annealed at 600 °C were used in all bioimaging experiments due to their high phase purity and attractive size distribution for intravascular applications.
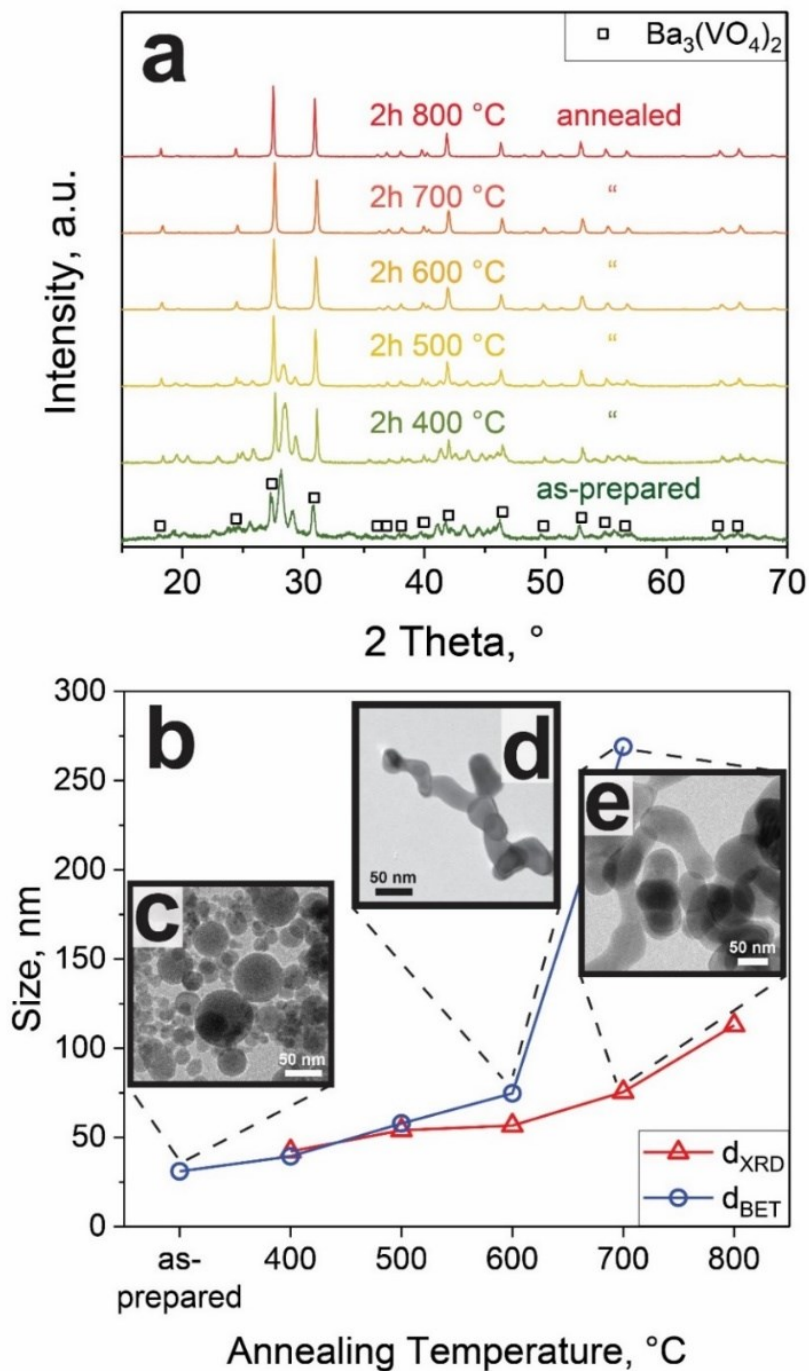
1

2 **Figure S1**: Structural characterization of $Ba_3(V_{0.995}Mn_{0.005}O_4)_2$: **a)** XRD patterns of as-
3 prepared and annealed particles and **b)** crystal (d_{XRD}, triangles) and primary particle sizes
4 (d_{BET}, circles). Inset: TEM images of particles: **c)** as-prepared, **d)** annealed for 2h at 600 °C in
5 air and **e)** annealed at 700 °C.
6
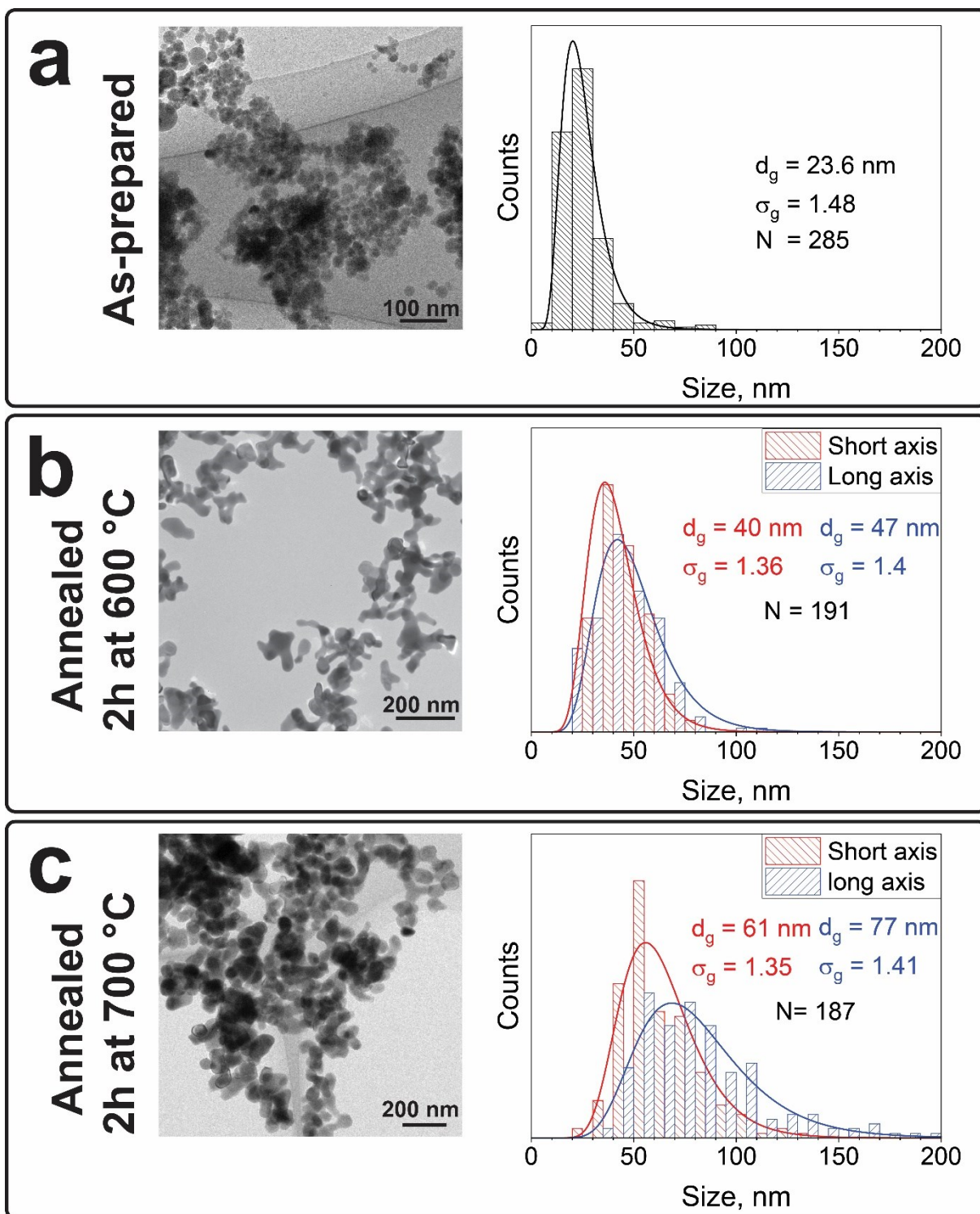
Figure S2: TEM images and size distributions of BaVOMn ($Ba_3(V_{0.995}Mn_{0.005}O_4)_2$) **a)** as-prepared, **b)** annealed at 600 °C and **c)** at 700 °C. Since the annealed particles were elongated, both their shortest and longest axis were evaluated. The geometric mean size (d_g) and geometric standard deviation (σ_g) are also given together with number of counted particles (N).

To optimize the emission intensity, the influence of Mn^{5+} doping concentration was investigated. The XRD patterns of $Ba_3(V_{1-x}Mn_xO_4)_2$ for x = 0 to 1 are shown in Figure S3.

1 Manganese can readily replace Vanadium atoms due to their similar ionic radii (Mn^{5+}: 33 pm,

2 V^{5+}: 35.5 pm[66]), enabling the full series of solid solutions[67] from $Ba_3(VO_4)_2$ to $Ba_3(MnO_4)_2$.

3 The integration into the crystal is further corroborated by analysis of the lattice parameter

4 (Figure S4): Replacing V^{5+} with smaller Mn^{5+} leads to a reduction of the cell parameter a and

5 the total unit cell volume.[67] Additionally, the concentration of Mn in the particles determined

6 by ICP-OES was in reasonable agreement with their nominal values (Figure S5).

7
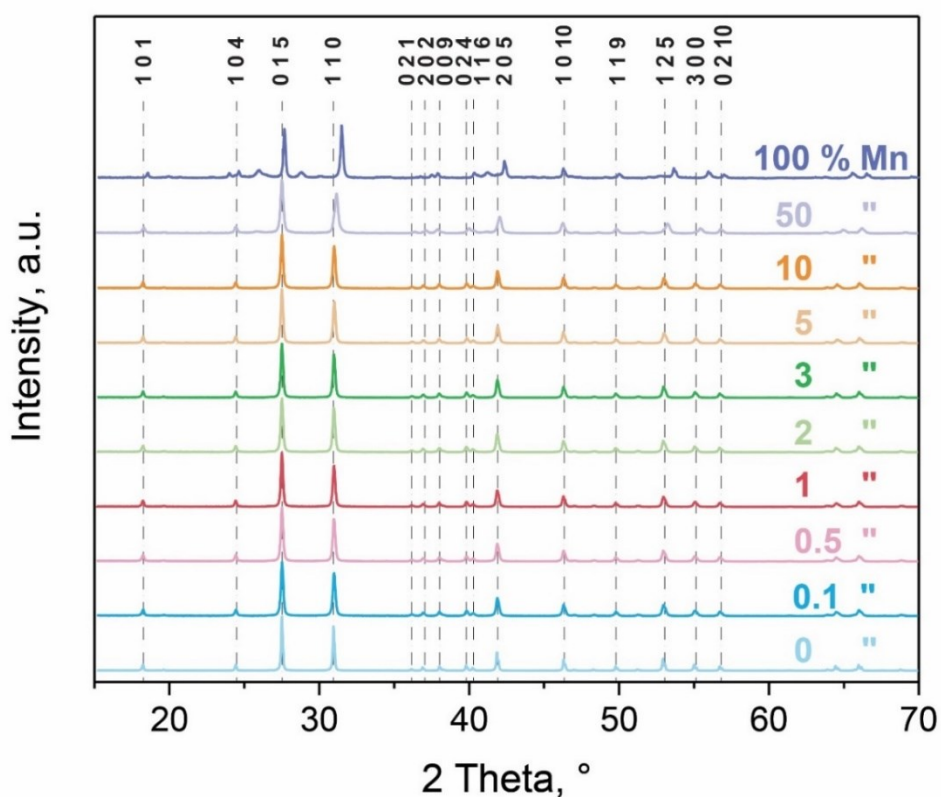
8

9 **Figure S3:** XRD patterns of $Ba_3(V_{1-x}Mn_xO_4)_2$ annealed for 2 h at 600 °C. The peaks are
10 labelled according to the reference pattern of $Ba_3(VO_4)_2$. For 100 % Mn, a second phase was
11 observed at 26 and 28 °.

1
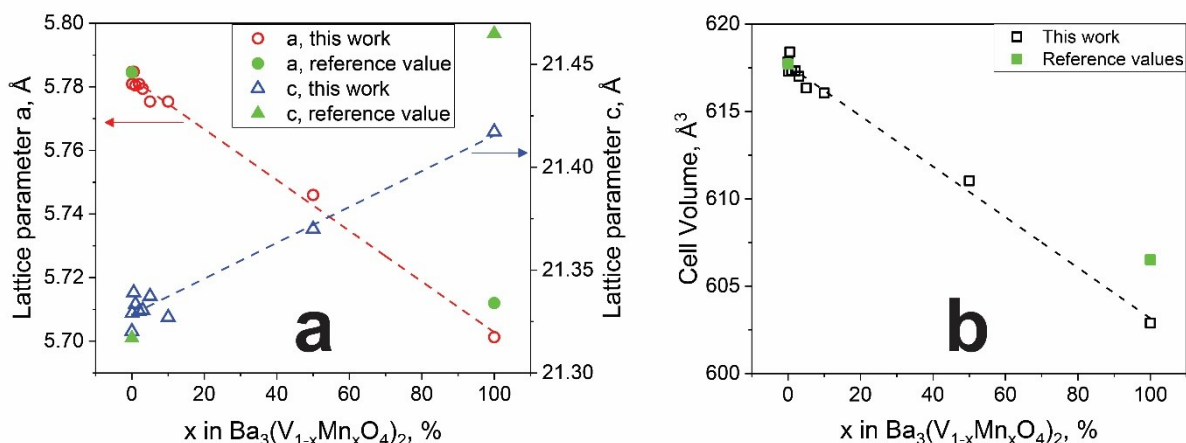
Figure S4: a) Lattice parameters a (circles) and c (triangles) and **b)** cell volume of $Ba_3(V_{1-x}Mn_xO_4)_2$ annealed for 2 h at 600 °C. The replacement of V^{5+} with the smaller Mn^{5+} leads to a continuous reduction of cell volume. The values are in good agreement with the crystallographic references (full symbols) for $Ba_3(VO_4)_2$ (PDF = 29-0211) but deviate for large Mn^{5+} contents from the $Ba_3(MnO_4)_2$ reference (PDF = 23-1026).


7
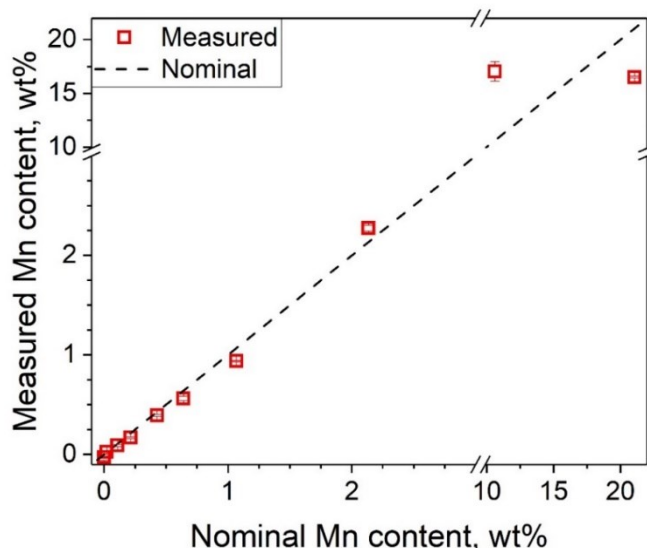
Figure S5: Manganese content of $Ba_3(V_{1-x}Mn_xO_4)_2$ measured by ICP-OES. The agreement with the nominal values is good up to 2.1 wt% (10 mol%), and deviates more for 10.6 and 21.1 wt% (50 and 100 mol% respectively).

The powder color (Figure S6a and inset Figure S6c) changes from white (x = 0) over sky blue to dark green (x = 0.5 and 1), confirming the Mn^{5+} valence state.[68] The corresponding absorption spectra (Figure S6b) reveal an increase in the NIR absorption with increasing Mn concentration.
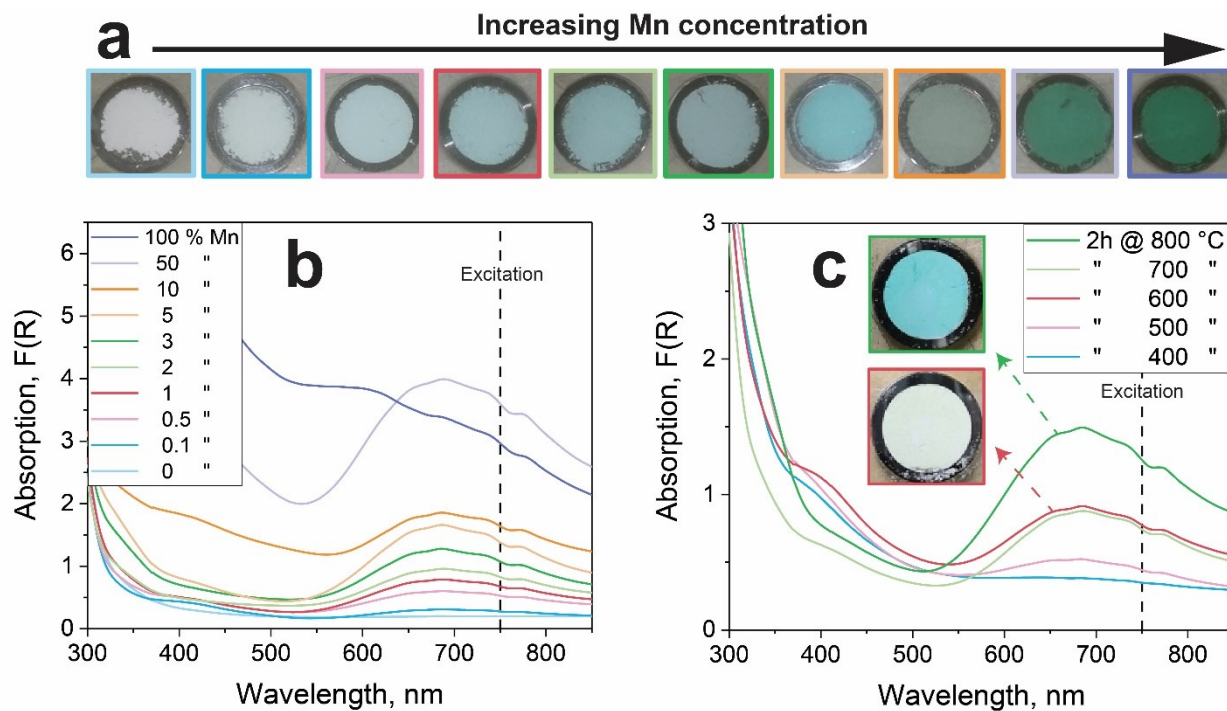
Figure S6: a) Powder images and **b)** absorption spectra of $Ba_3(V_{1-x}Mn_xO_4)_2$ annealed for 2 h at 600 °C and **c)** $Ba_3(V_{0.995}Mn_{0.005}O_4)_2$ annealed at different temperatures. Not all of the Mn-dopant is present in the pentavalent state after particle synthesis, and annealing increases the amount of Mn^{5+} in the particles.

The energy levels of Mn^{5+} in a strong crystal field can be described by the Tanabe-Sugano diagram (Figure S7). There are three spin-allowed transitions from the $^3A_2$ ground state that dominate the excitation and absorption spectra (Figures S8 and S10a): The $^3A_2 \rightarrow {}^3T_2$ transition at 888 nm, the $^3A_2 \rightarrow {}^3T_1(^3F)$ at 654 nm and the $^3A_2 \rightarrow {}^3T_1(^3P)$ transition at 341 nm.[69] Additionally, there is also a weaker spin-forbidden transition at 777 nm corresponding to $^3A_2 \rightarrow {}^1A_2$, and a charge transfer (CT) band from the host that overlaps with the $^3A_2 \rightarrow {}^3T_1(^3P)$ transition.

1
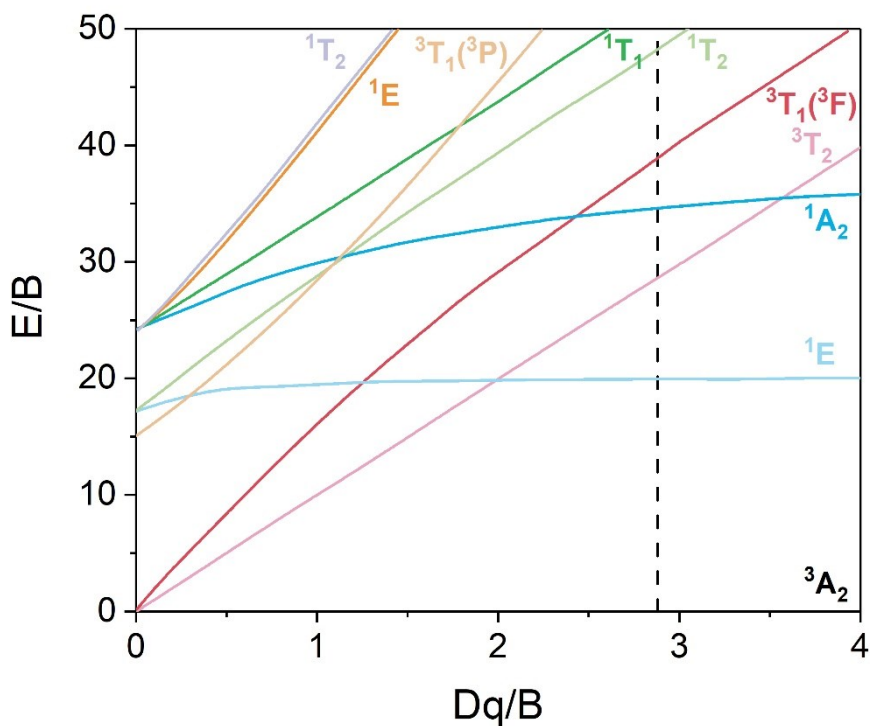
Figure S7: Tanabe-Sugano diagram for tetrahedrally coordinated $3d^2$ ions (Figure adapted from Svelto et al.[70]) The dashed line corresponds to a Racah parameter (Dq/B) of 2.88, which has been determined for Mn^{5+} in $Ba_3(VO_4)_2$ analogous to Zhang et al.[71]

5

6
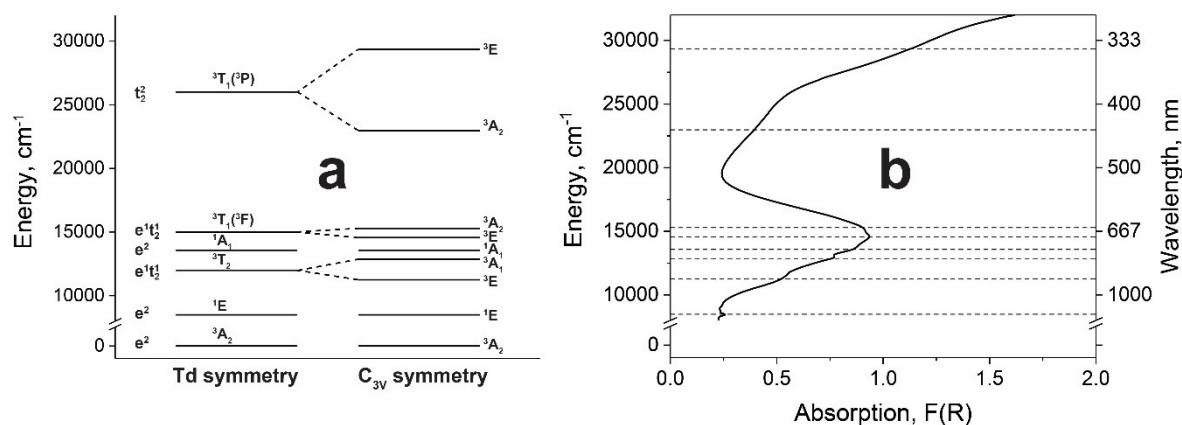
Figure S8: a) Energy diagram for Mn^{5+} in a tetrahedral crystal field (Td) and effects of lowering the symmetry (C_{3v}), as in $Ba_3(VO_4)_2$ (adapted from Dardenne[69]). **b)** UV-VIS spectrum of BaVOMn ($Ba_3(V_{0.995}Mn_{0.005}O_4)_2$, annealed at 800 °C) with the corresponding transitions to a).
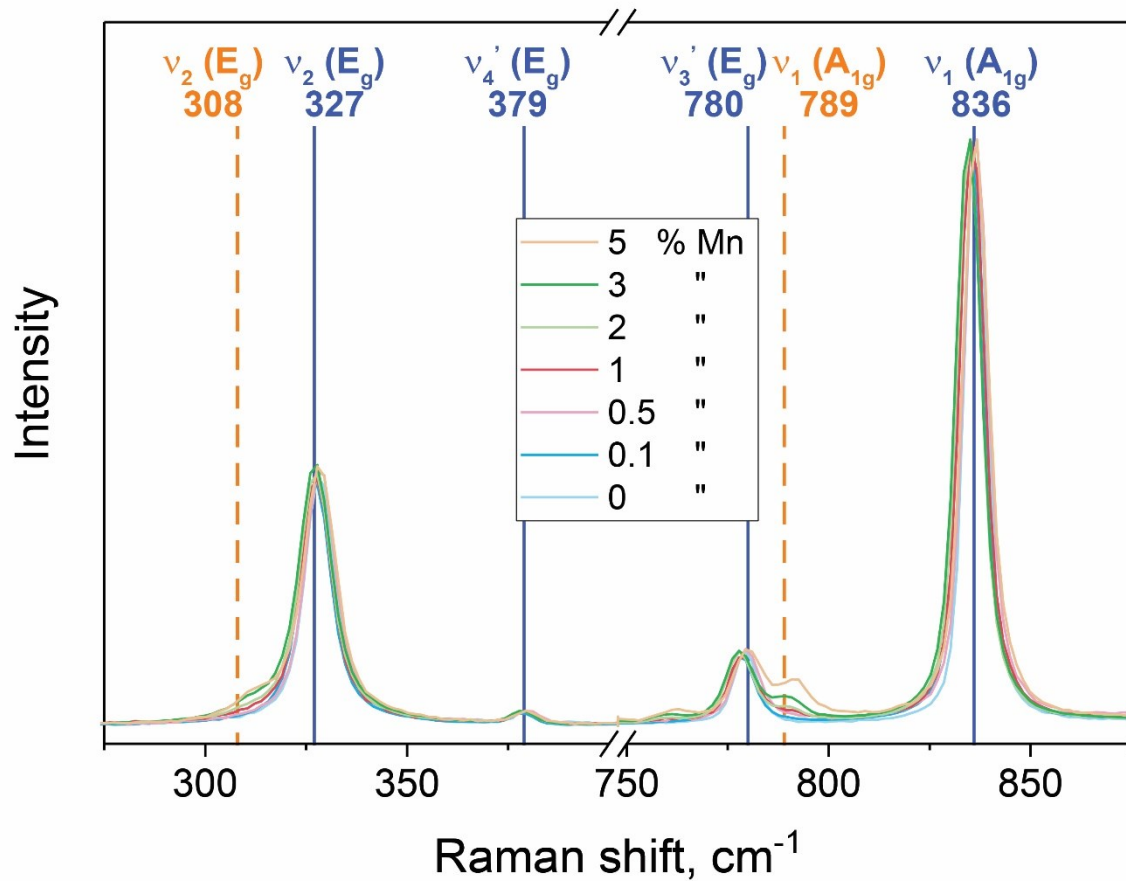
1
2 **Figure S9:** Raman spectra of $Ba_3(V_{1-x}Mn_xO_4)_2$. Solid lines can be attributed to vibrations
3 originating[72] from $Ba_3(VO_4)_2$. With increasing Mn content, two additional peaks arise at 308
4 and 789 cm^{-1} (dashed lines) that can be assigned[73] to MnO_4^{3-} group (or Mn^{5+}).
5
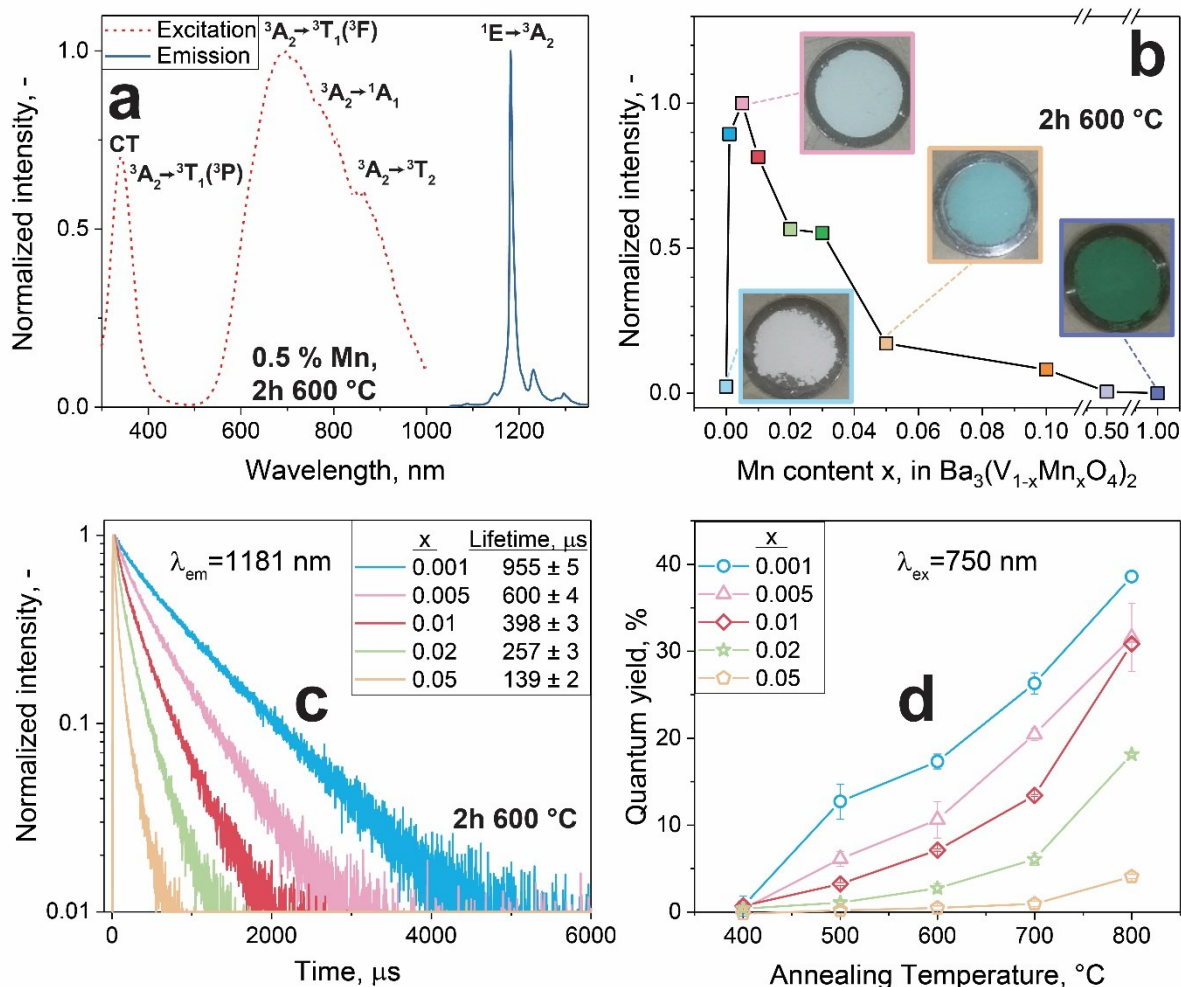
Figure S10: a) Excitation (λ_{em} = 1181 nm, dotted line) and emission spectra (λ_{ex} = 750 nm, solid line) of $Ba_3(V_{0.995}Mn_{0.005}O_4)_2$ after annealing in air for 2h at 600°C **b)** Effect of Mn concentration on the luminescence of particles annealed at 600 °C and dispersed in water (0.5 g/L) (Inset: Powder images) **c)** Fluorescence decays of powders with different Mn doping content x (annealed at 600 °C) **d)** Quantum yield as a function of annealing temperature of powders at various doping contents.

The emission intensity of aqueous dispersions of these particles (Figure S10b) goes through an optimum at 0.5 % Mn content (x = 0.005) and decreases for higher ones, reaching almost zero for 50 and 100 %. This is in good agreement with studies[74] on $Ba_3(VO_4)_2$ and $Ba_3(PO_4)_{2,}$[75] reporting an optimal concentration of 1%. While the increase for low Mn contents is related to higher number of active centers, the subsequent reduction of emission intensity for x > 0.005, despite increased absorption, can be attributed to concentration quenching due to increased probability of non-radiative energy transfer between neighbouring Mn^{5+} ions.[76]

1	This is further supported by fluorescence decay measurements of the 1181 nm emission

2	(Figure S10c). All decays exhibit a bi-exponential decay, similar to Mn^{5+}-doped silicates[71]

3	(fitting parameters given in Table S1). With increasing Mn concentration, the average lifetime

4	decreases, indicative of an enhanced cross relaxation and energy transfer rate between Mn^{5+}

5	due to higher dopant concentration.[71] Furthermore, the higher doping concentration reduces

6	the crystal symmetry and leads to a decreased energy separation between the $^3T_2$ and ^1E level,

7	which favours the $^3T_2 \rightarrow {}^3A_2$ multiphonon relaxation[77] (Figure S7). The average fluorescence

8	lifetime is highest for x = 0.001 with 955 µs and decreases down to 139 µs for x = 0.05. These

9	lifetimes are considerably higher than those of $Ba_3(VO_4)_2$, (e.g. 364 µs for x = 0.00021[74], 480

10	µs for x = 0.002[78], and 450 µs for x = 0.002[24]). Such long and tunable fluorescence lifetimes

11	can be advantageous for bioimaging using time-gated fluorescence to remove

12	autofluorescence[79] or for multiplexed imaging.[80]

13	Next, the efficiency of these particles is studied in detail with their quantum yield (QY).

14	The result of the absolute QY measurements with an integrating sphere (Figure S12) for

15	different dopant concentrations as a function of annealing temperatures is shown in Figure

16	S10d. The lowest Mn concentration shows the highest QY at all annealing temperatures, in

17	agreement with fluorescence lifetime analysis (Figure S10c). Furthermore, the QY increases

18	for all dopant concentrations with annealing temperature. Interestingly, the brightness is

19	almost linear with the crystal size (Figure S11a), regardless of dopant concentration (Figure

20	S11b). This is caused most likely by increased crystal phase purity and reduced surface-

21	defects[81] due to the reduced surface to volume ratio of larger particles. Additionally, the

22	powder samples became darker and more intense blue with increasing annealing temperature

23	(Fig. S6c). This indicates that not all of the Mn-dopant was present in the pentavalent state in

24	the as-prepared particles and that the Mn^{5+} can be stabilized by heating. Most importantly, the

25	particles reach a quantum yield up to 39 %, which is among the highest reported for this

1 spectral region, on par with quantum dots, as detailed in Table S1. As the emission intensity

2 was highest for x = 0.005 (Figure 10b), this composition was selected for further evaluation

3 and labeled BaVOMn for brevity. Its QY (annealing temperature of 600 °C) in aqueous

4 dispersion was 4.6 ± 1.1 %.
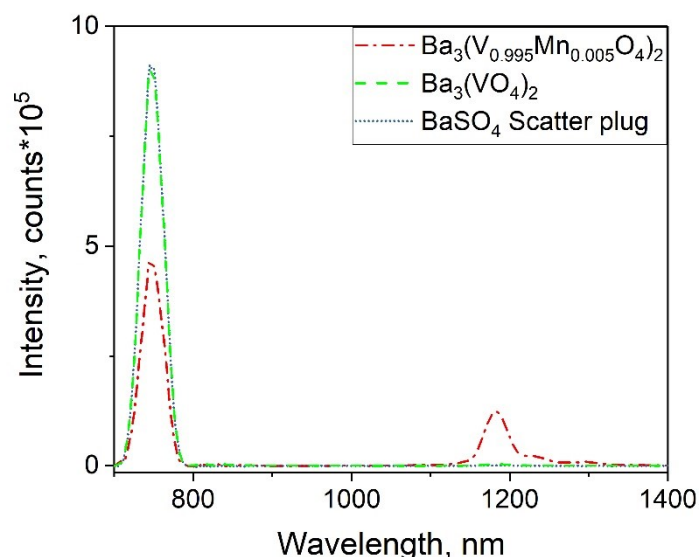
5
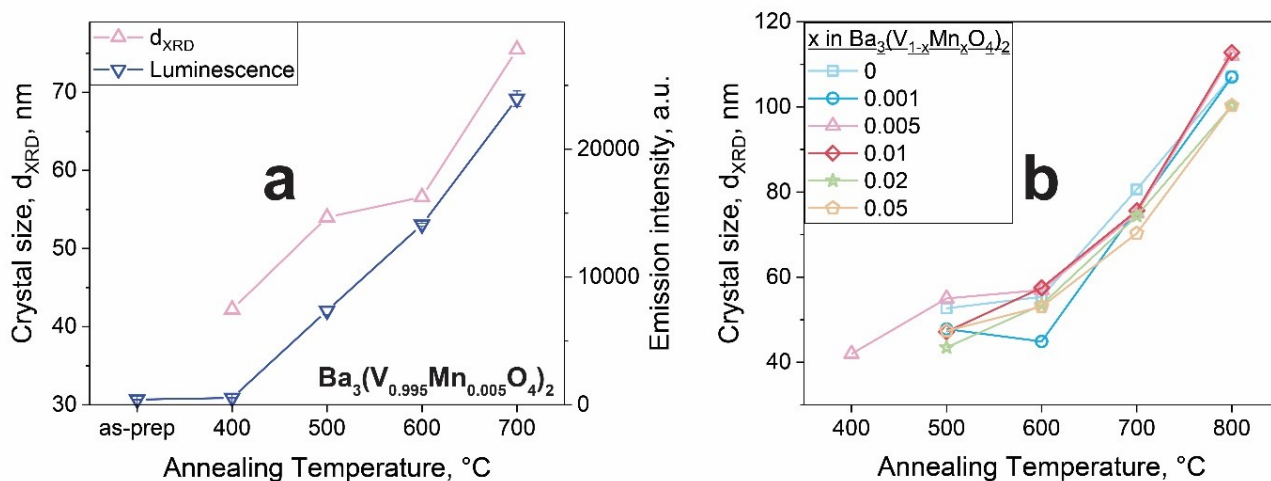
6

7 **Figure S11: a)** Luminescence intensity of aqueous solutions and crystal sizes of BaVOMn as
8 a function of annealing temperature. The emission intensity depends on crystal size.[81] **b)**
9 Crystal size as a function of annealing temperature for several Mn contents. The Mn-
10 concentration does not affect the crystal size within this concentration range.

11

12
13 .

1

2 **Figure S12:** Exemplary spectrum for determination of quantum yield. The QY was calculated

3 by $QY = \dfrac{Emitted\ Photons}{Absorbed\ Photons} = \dfrac{\int_{1050nm}^{1400nm} I_{sample} - \int_{1050nm}^{1400nm} I_{reference}}{\int_{700nm}^{800nm} I_{reference} - \int_{700nm}^{800nm} I_{sample}}$, where I represents the intensity at a

4 specific wavelength. As a reference, a strongly scattering $BaSO_4$ plug was placed inside the
5 integrating sphere, as $BaSO_4$ exhibited practically identical scattering intensity to pure
6 $Ba_3(VO_4)_2$.
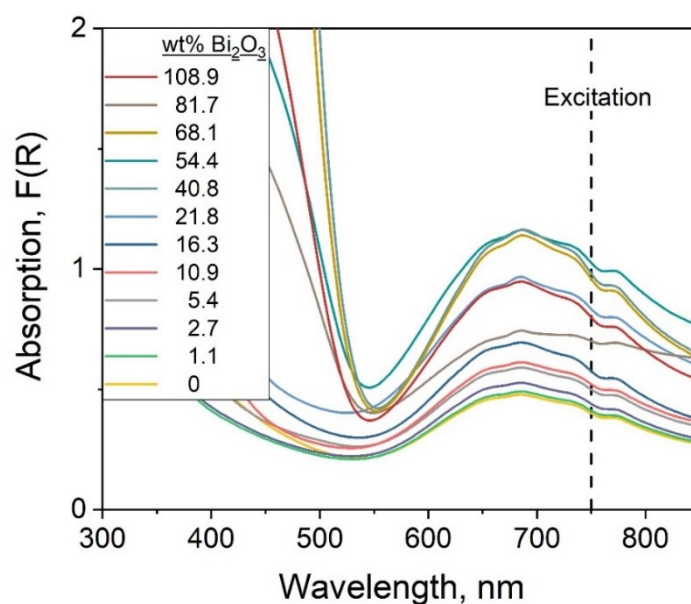
7

8 **Figure S13**: Absorption of BaVOMn – y wt% Bi_2O_3 annealed for 2h at 600°C. Higher Bi_2O_3
9 content leads to an increased absorption in the NIR (dashed line = 750 nm), indicating that
10 more Mn^{5+} is stabilized. For 54.4 wt% Bi_2O_3 and higher, the absorption of host material is
11 extended up to 500 nm, leading to the typical yellow[82] color for pure Bi_2O_3.

12 **SI-II: Optimization and characterization of $Ba_3(V_{0.995}Mn_{0.005}O_4)_2$-$Bi_2O_3$**
13 **nanoparticles**
14

1
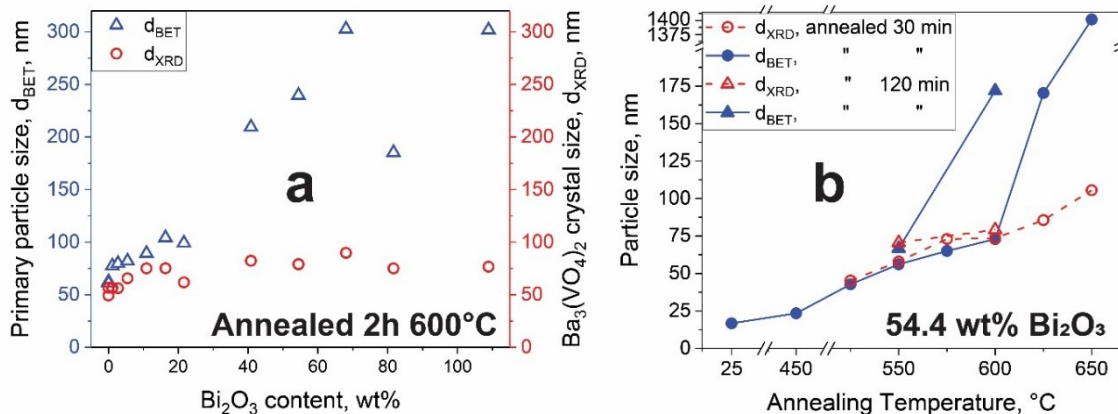
Figure S14: **a)** Primary particle (d_{BET}, triangles) and crystal sizes (d_{XRD}, circles) of Bi_2O_3
containing particles annealed for 2h at 600 °C in air. **b)** The effect of annealing temperature
on BaVOMn-BiO ($Ba_3(V_{0.995}Mn_{0.005}O_4)_2$-54.4wt% Bi_2O_3) d_{BET} and d_{XRD}.

5
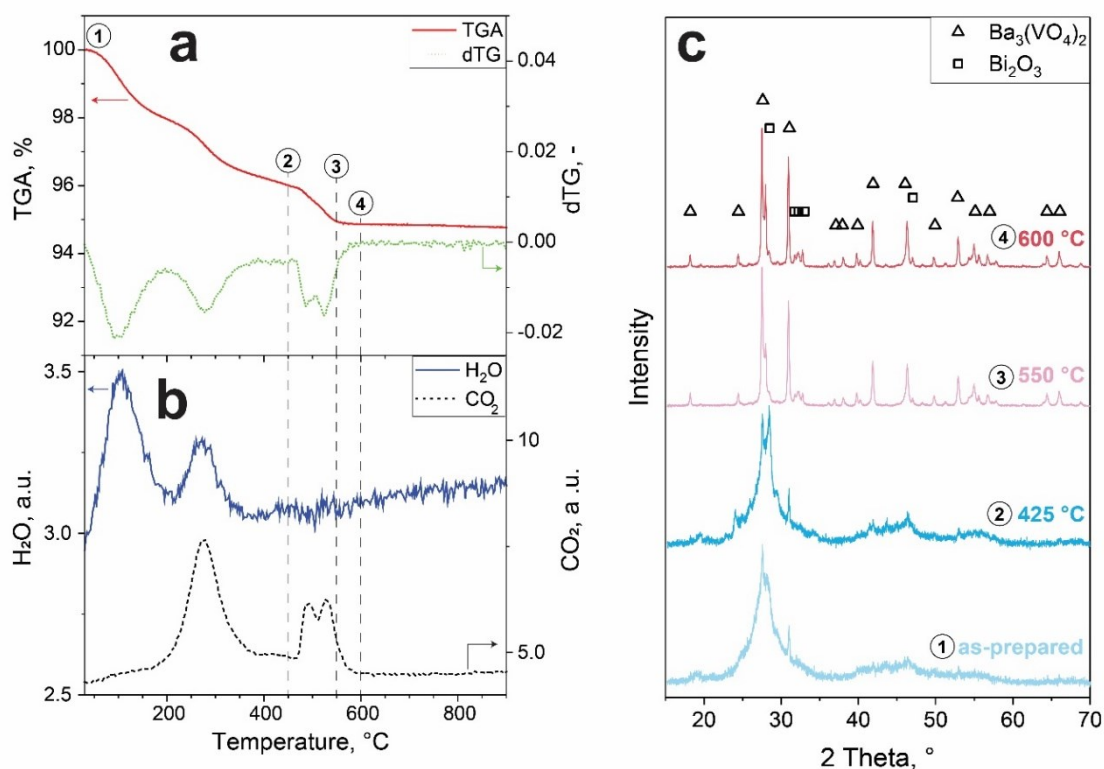
Figure S15: a) Thermogravimetric analysis of BaVOMn-BiO ($Ba_3(V_{0.995}Mn_{0.005}O_4)_2$-
54.4wt% Bi_2O_3) combined with **b)** mass spectroscopy of the evolved gases. A first weight
loss up to 200 °C corresponds to adsorbed water. A second mass loss around 270 °C could be
related to removal of organics such as any uncombusted precursor residues. **c)** XRD pattern at
different annealing temperatures (holding time = 30 min).
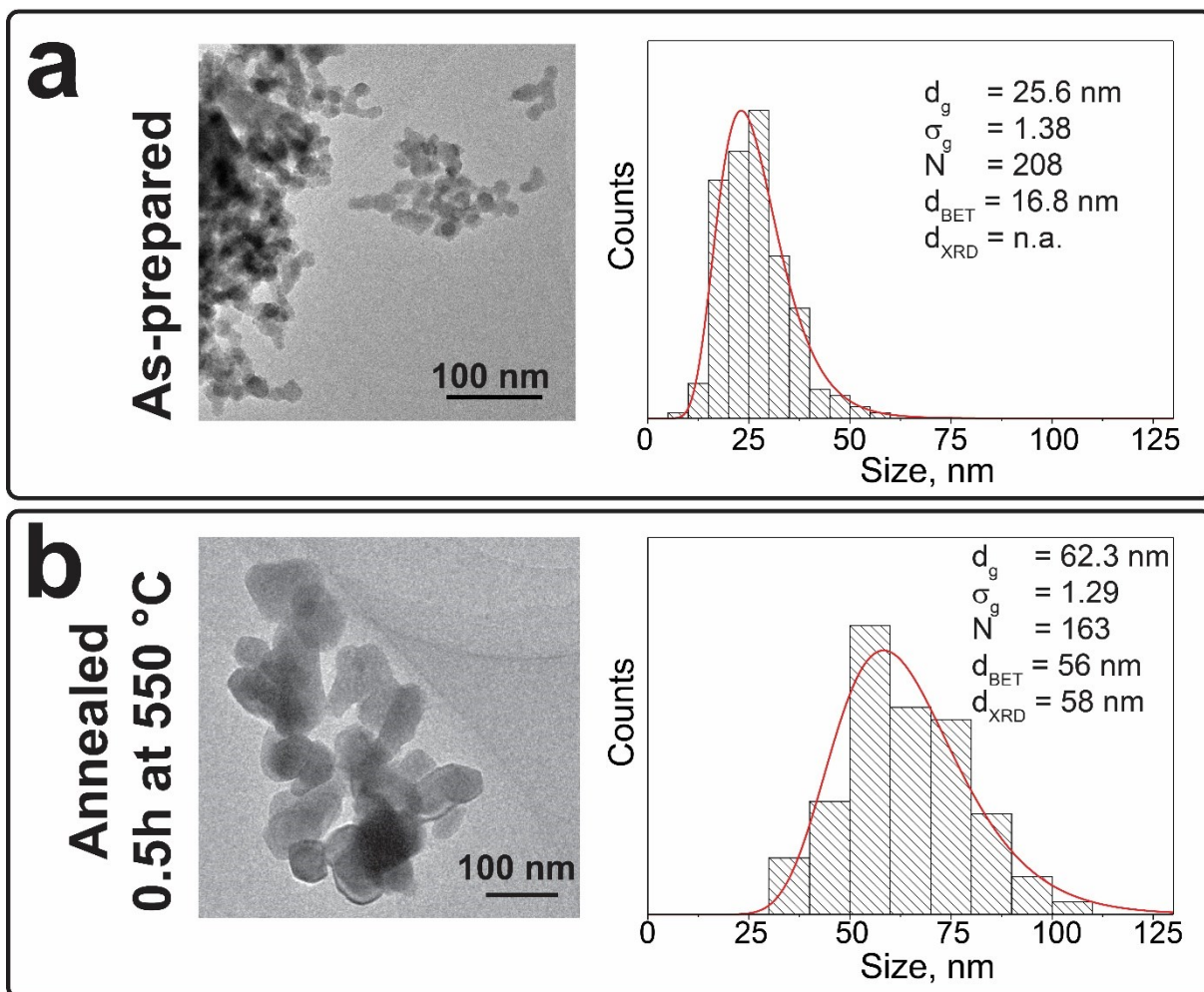
Figure S16: TEM images and size distributions of BaVOMn-BiO ($Ba_3(V_{0.995}Mn_{0.005}O_4)_2$-54.4wt% Bi_2O_3) **a)** as-prepared and **b)** annealed at 550°C for 30 minutes. The geometric mean size (d_g) and geometric standard deviation (σ_g) are also given together with number of counted particles (N), as well as the primary particle (d_{BET}) and crystal size (d_{XRD}).
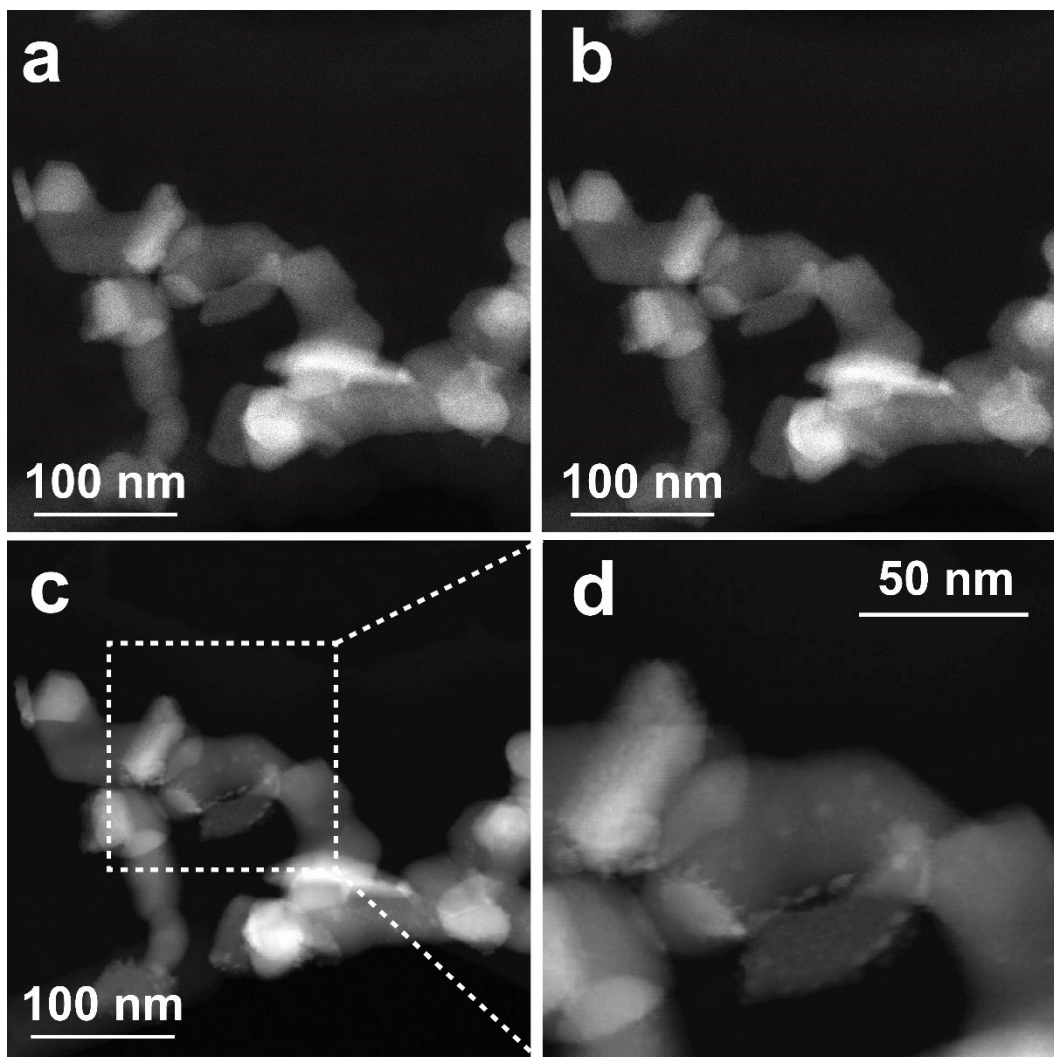
Figure S17: Assessment of the effect of an electron-beam on the sample at liquid nitrogen temperature. Using low electron dose rate allows for continuous scanning for 2 minutes without any significant alterations to the particles between the initial image **(a)** and after 2 minutes **(b)**. However, after switching to higher e-dose rates that are required for elemental mapping, the particle morphology is affected within seconds and small metallic Bi-spots are formed **(c),** magnified in **(d).**
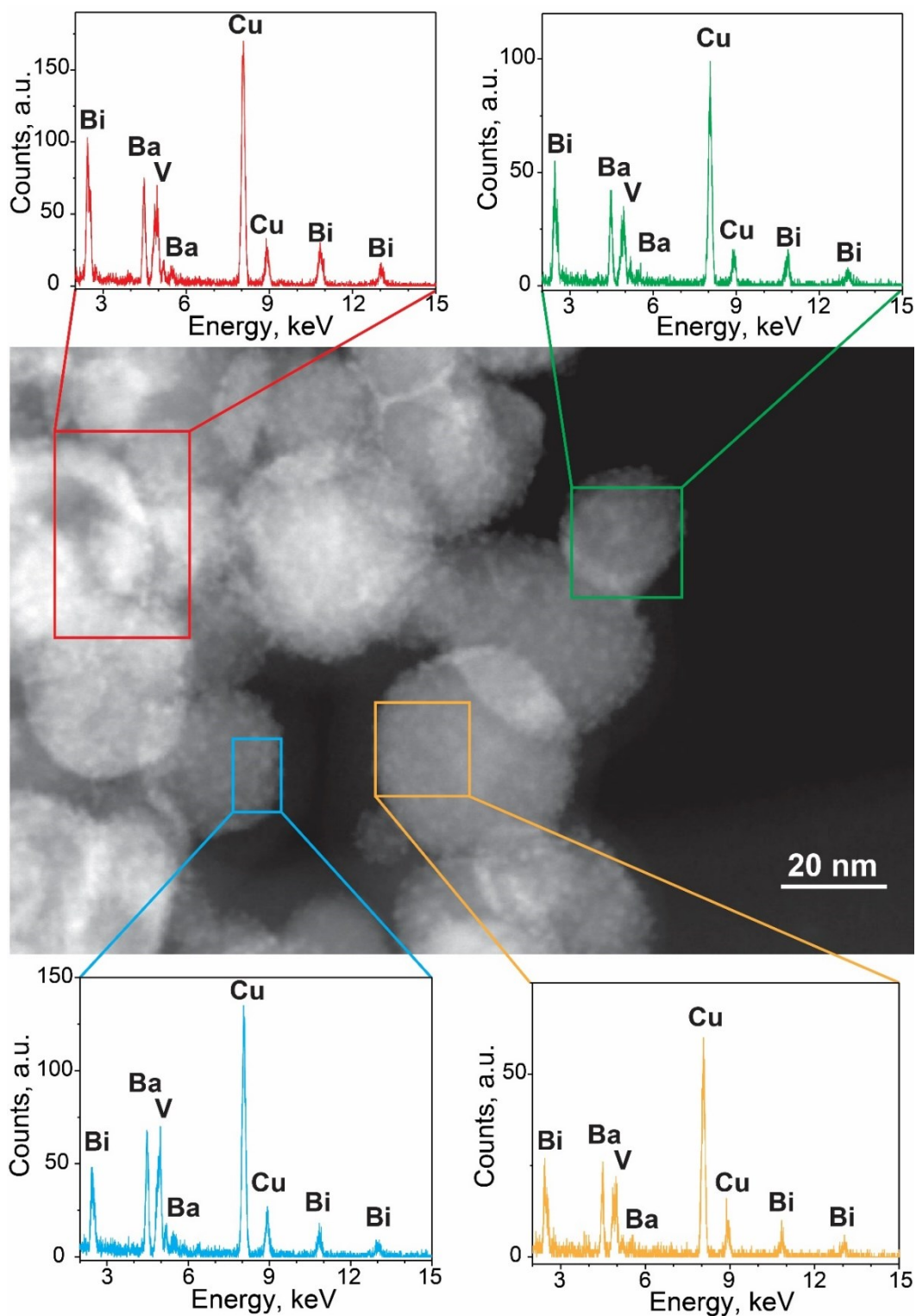
1

2 **Figure S18**: HAADF-STEM of as-prepared BaVOMn-BiO particles with EDX spectra of
3 selected areas. No separate Bi_2O_3-containing areas can be observed. The dots on the particle
4 surface come from the formation of Bi-particles due to interaction of the electron beam with
5 the sample during STEM. Cu signal originates from the TEM copper grid.
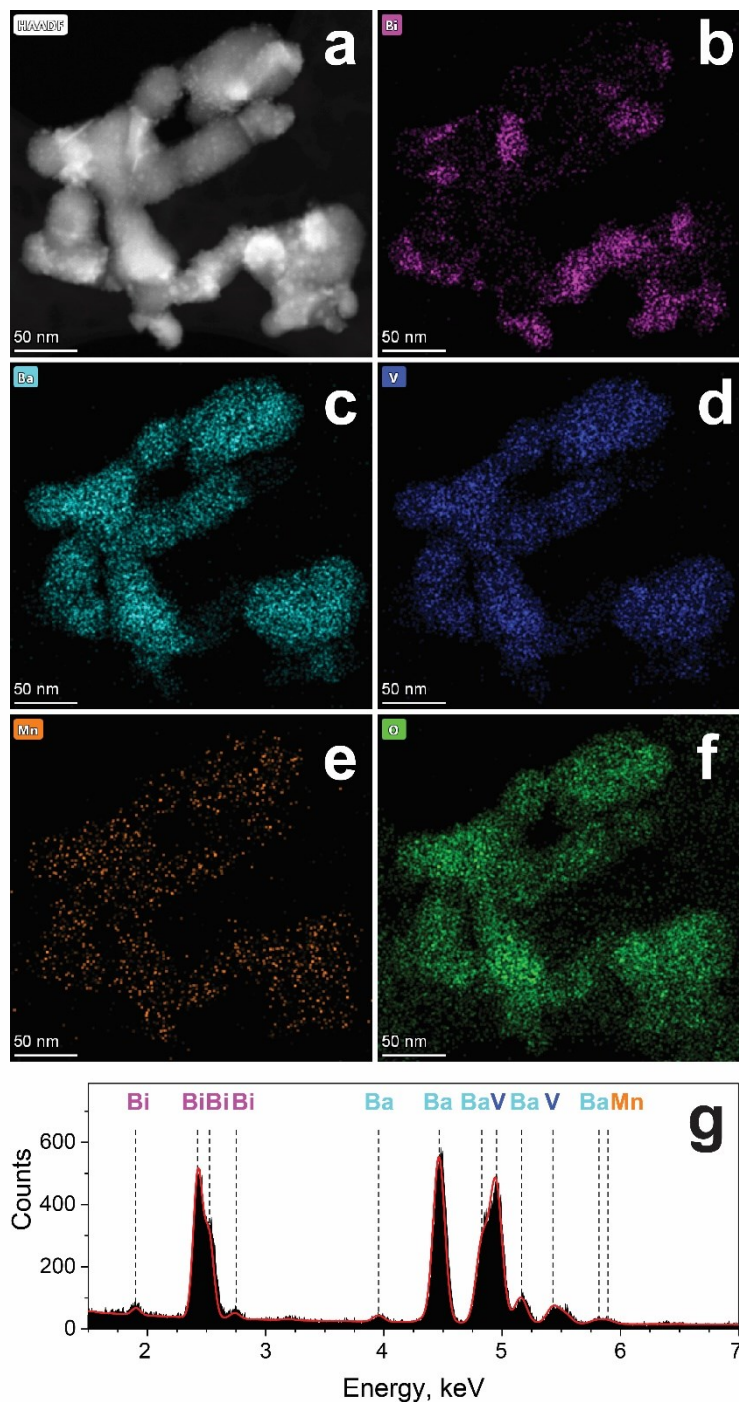
Figure S19: Electron microscopy with energy-dispersive X-ray analysis of annealed (30 min @ 550 °C) BaVOMn-BiO. **a)** HAADF-STEM, corresponding elemental mappings of **b)** Bi, **c)** Ba, **d)** V, **e)** Mn, and **f)** O, and **g)** an EDX spectrum of the entire area. The mapping of Mn needs to be considered with care due its low concentration (and associated EDX peak intensity) as well as partial overlap with barium (at 5.797 keV), as shown in the EDX spectrum (g).

1
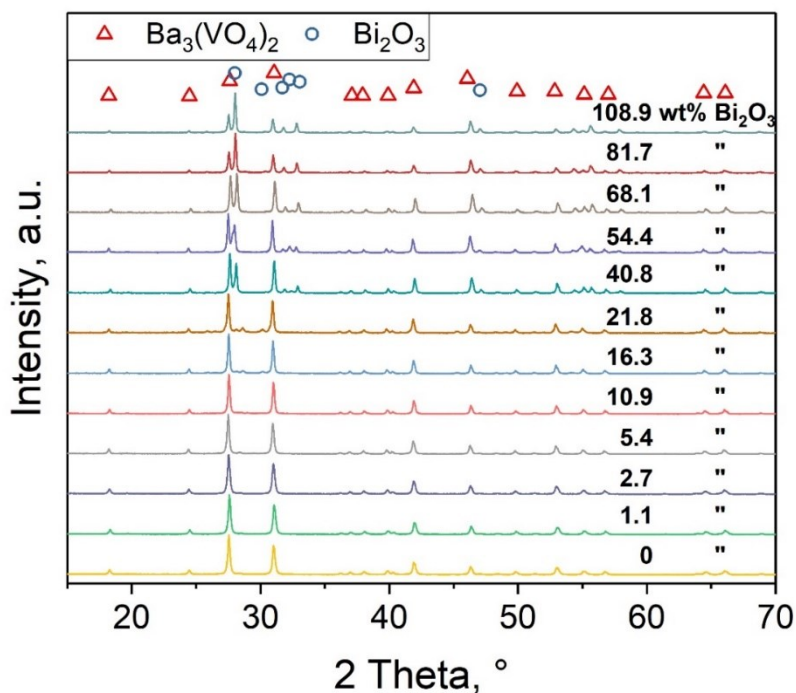
Figure S20: Normalized XRD patterns of co-oxidized $Ba_3(V_{0.995}Mn_{0.005}O_4)_2 - y$ wt% Bi_2O_3 annealed for 2 h at 600 °C. For higher Bi_2O_3 contents (> 5.4 wt%), a tetragonal Bi_2O_3 phase can be clearly identified at $2\theta = 28$ °.

5
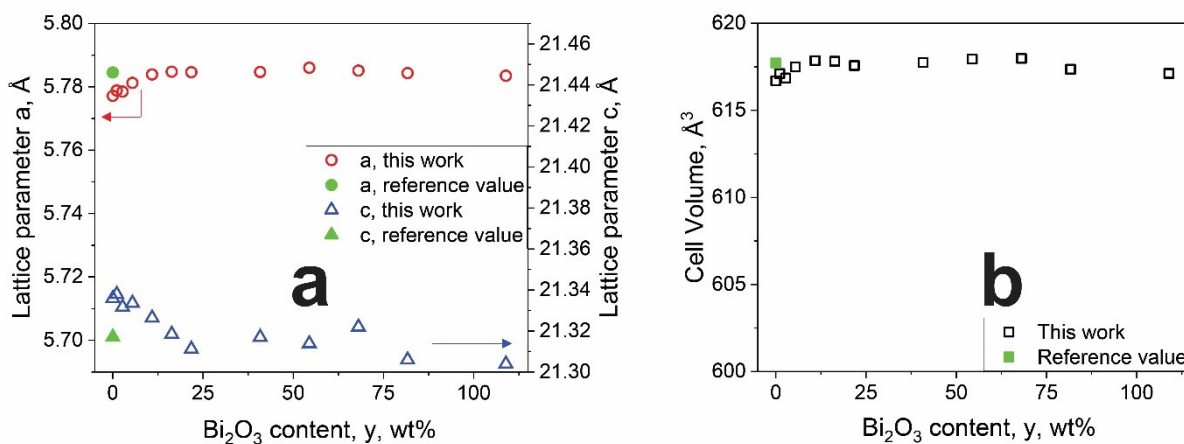
Figure S21: **a)** Lattice parameters a (open circles) and c (open triangles) of $Ba_3(V_{0.995}Mn_{0.005}O_4)_2 - y$ wt% Bi_2O_3 and **b)** cell volume. For comparison, the reference values of $Ba_3(VO_4)_2$ (PDF = 29-0211) are given too (filled symbols). Only a slight change in the unit cell is observed up to 10.9 wt% of Bi_2O_3 in agreement with the appearance of separate Bi_2O_3 peaks in the XRD spectra (Figure S20).

1
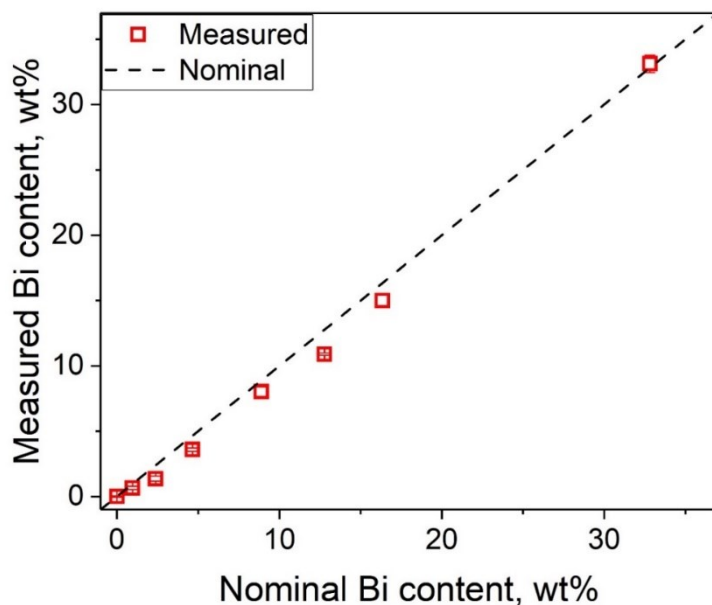
Figure S22: Bismuth (Bi) content of $Ba_3(V_{0.995}Mn_{0.005}O_4)_2 - y$ wt% Bi_2O_3 particles analyzed by ICP-OES. The measured values are in good agreement with the nominal ones.

4

5
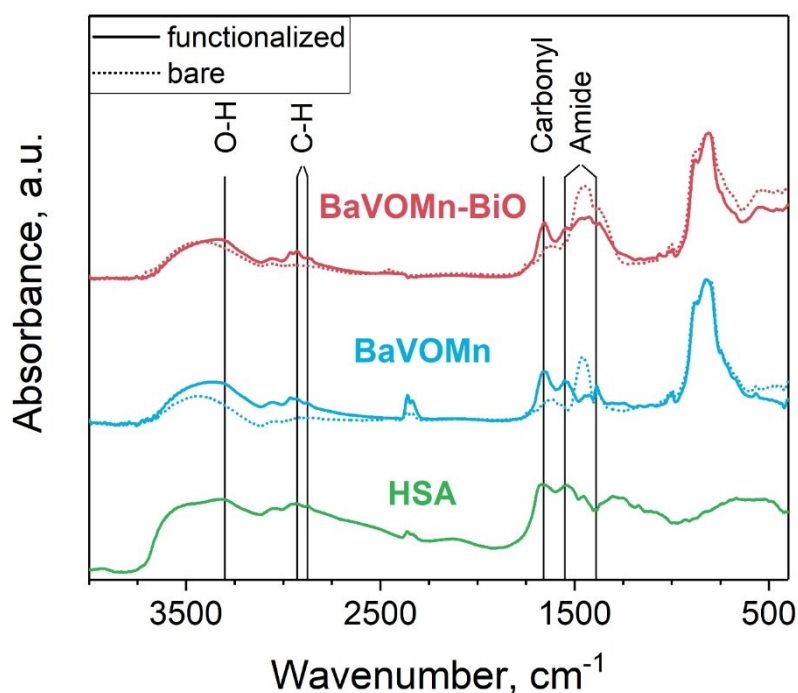
Figure S23: Normalized FTIR spectra of pure HSA, as well as bare (dotted lines) and HSA-functionalized (solid lines) BaVOMn and BaVOMn-BiO. The main characteristic peaks of pure HSA (marked with black solid lines) correspond to O-H (3300 cm^{-1}), C-H (2930 and 2875 cm^{-1}), carbonyl (1660 cm^{-1}) and amide (1550 and 1390 cm^{-1}) groups.[83] The presence of these characteristic peaks in the HSA-functionalized samples indicates successful attachment.

11
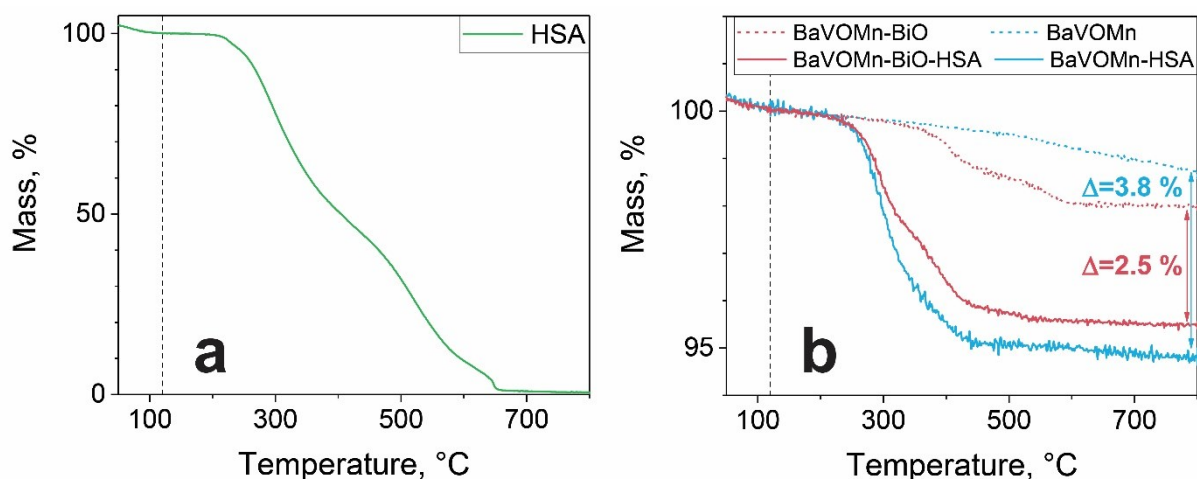
1

2 **Figure S24:** Thermogravimetric analysis under ambient air of **a)** pure HSA and **b)** bare (dotted
3 lines) and HSA-functionalized (solid lines) BaVOMn and BaVOMn-BiO. Pure HSA is
4 completely decomposed at 650 °C. The bare particles exhibit a small mass loss only (< 2 %).
5 The amount of HSA was quantified by calculating the difference (Δ) between bare and
6 functionalized particles, resulting in a coating density of 2.4 and 1.5 mg_{HSA}/m^2 for BaVOMn
7 and BaVOMn-BiO, respectively. Similarly, a coating density of 3.4 mg_{HSA}/m^2 has been reported
8 for HSA-functionlized Bi_2O_3.[53]
9
10
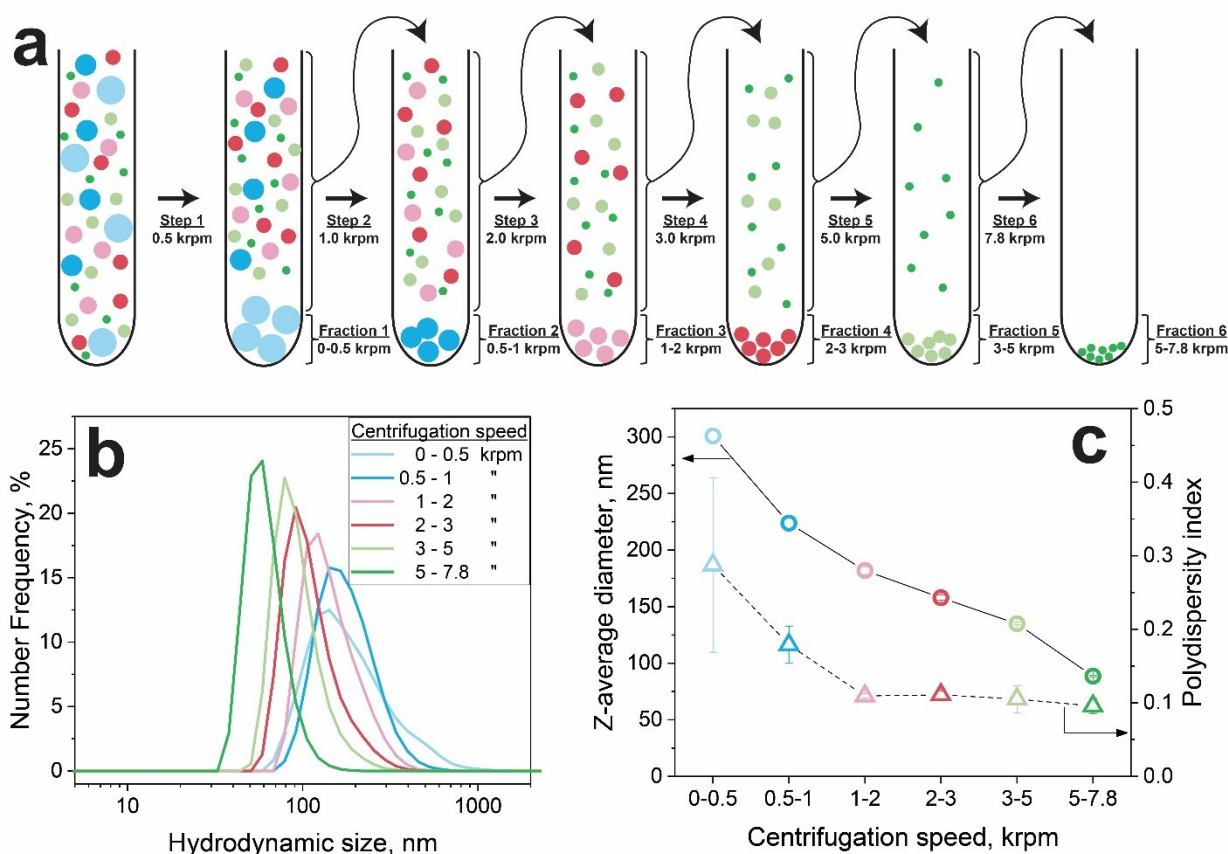
11

12 **Figure S25: a)** Centrifugation-separation sequence of HSA-functionalized BaVOMn-BiO
13 particles annealed for 30 minutes at 550 °C. Particles of different hydrodynamic sizes were
14 separated by taking the supernatant after centrifugation at different speeds of aqueous

1 dispersions of particles. **b)** DLS size distributions of the different fractions and **c)**
2 corresponding Z-average size and polydispersity index.

3
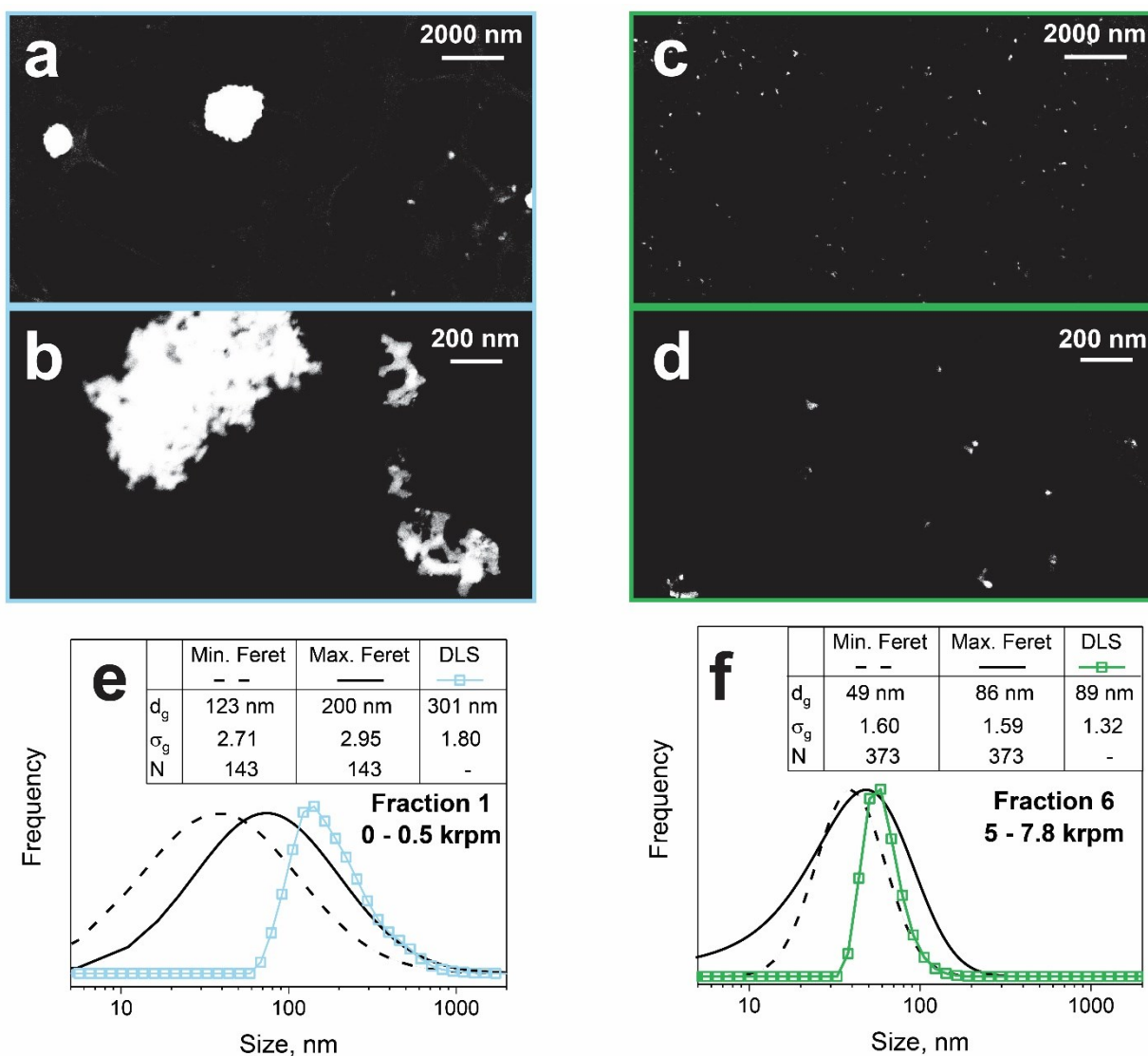
Figure S26: HAADF-STEM images at two magnifications of HSA-functionalized BaVOMn-BiO particles annealed for 30 minutes at 550 °C after separating fractions at 0 – 0.5 krpm (**a & b**) and 5 – 7.8 krpm (**c & d**) centrifugation speeds. Size distributions of the smallest (dashed black lines) and largest aggregate Feret diameter (solid black lines), along with the ones from DLS (line with symbols) for **e**) Fraction 1 (0 – 0.5 krpm) and **f**) Fraction 6 (5 – 7.8 krpm). The insets give their geometric mean (d_g) and standard deviation (σ_g), as well as the number of counted particles (N). High centrifugation speeds remove larger aggregates, resulting in narrower size distribution with smaller mean particle size.
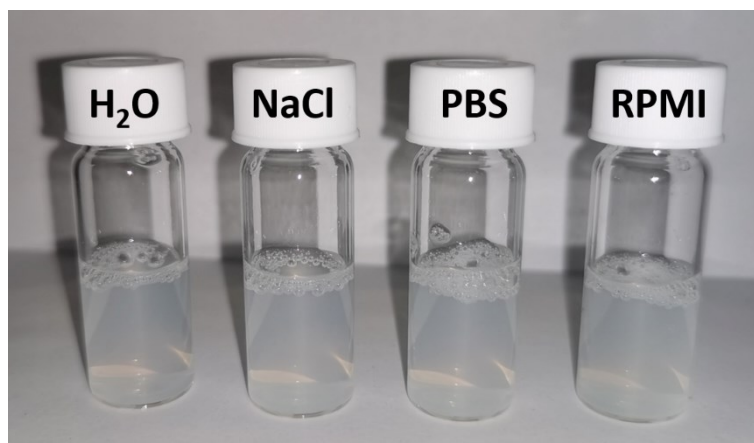
Figure S27: Photographs of BaVOMn-BiO particles dispersed in H_2O, 0.154 M NaCl, PBS and RPMI cell culture medium at 0.2 g/l. No strong agglomeration is observed in these media, indicating good colloidal stability.
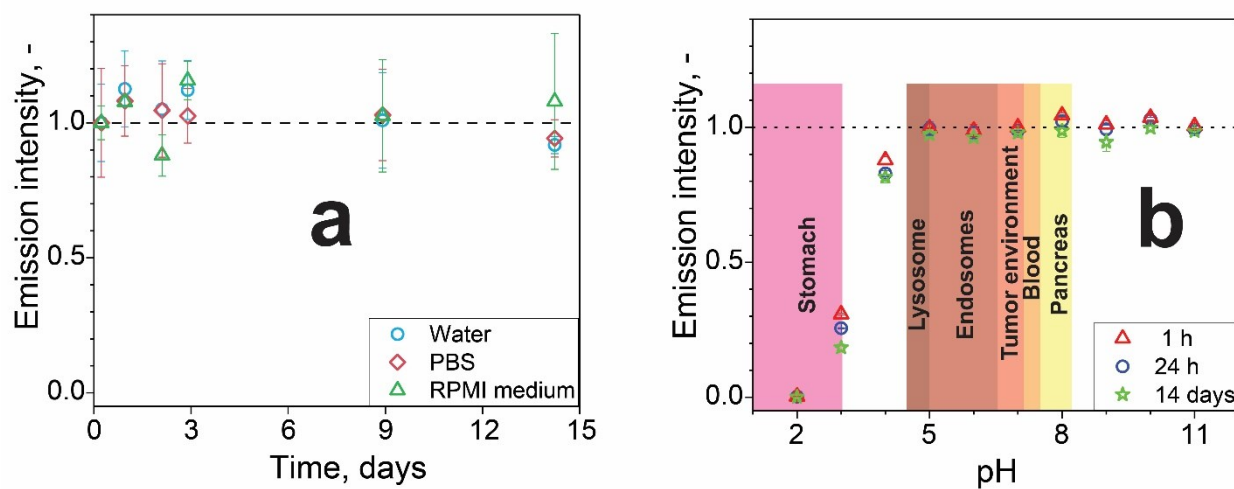
Figure S28: a) Fluorescence emission intensity in different media over 14 days. **b)** Emission intensity in aqueous solutions of various pH for 1 h, 24 h, and 14 days, along with common pH values found in the human body.
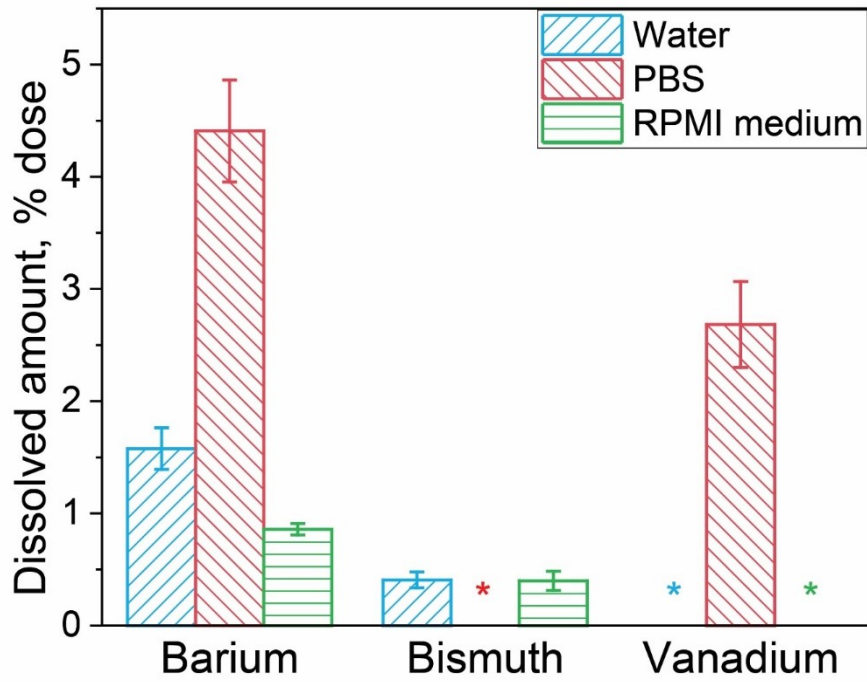
1

2 **Figure S29:** Dissolved or leached amount of barium, bismuth and vanadium ions from
3 BaVOMn-BiO particles after 14 days in different media. *: not detected.

4

5
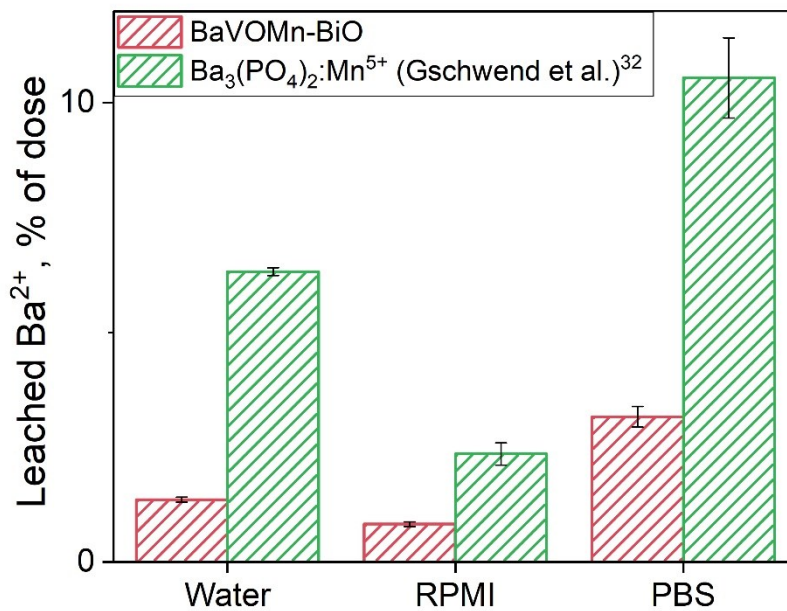
6

7 **Figure S30:** Comparison of leached Ba^{2+} from BaVOMn-BiO and $Ba_3(PO_4)_2$:Mn^{5+} after 24 h
8 in different media.

9

1
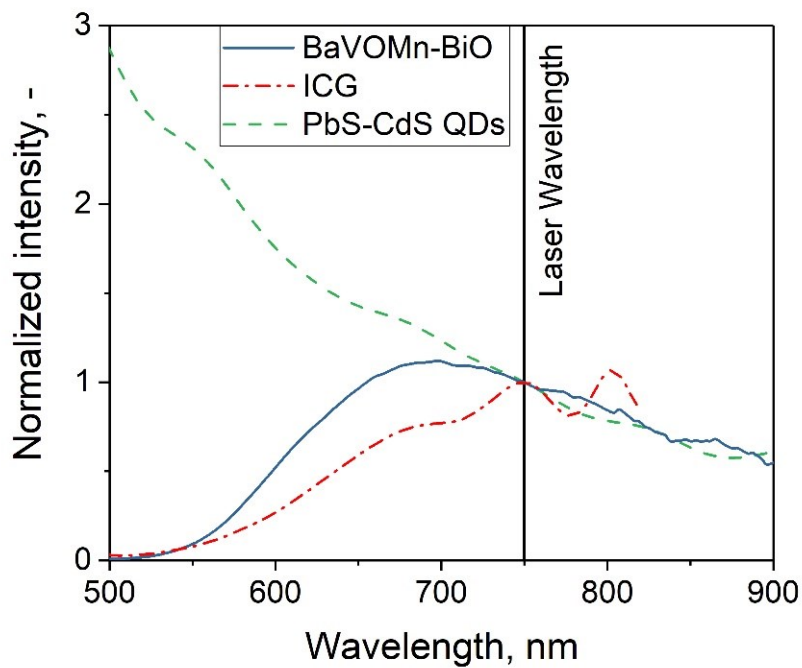
Figure S31: Excitation spectra of commercial ICG and PbS-CdS QDs, monitored at their peak
emission wavelength and normalized to 750 nm.

4

5
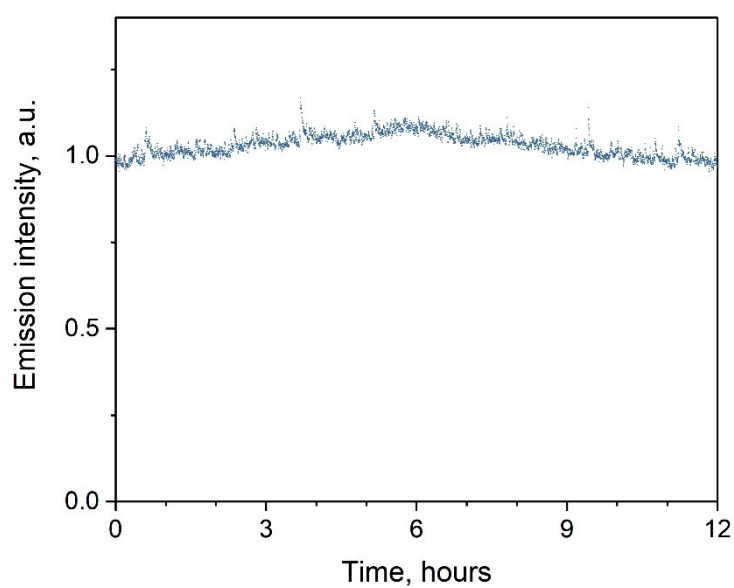
Figure S32: Photostability of BaVOMn-BiO particles annealed for 30 minutes at 550 °C in
water under constant laser irradiation (750 nm, 2.9 W/cm^2).

8

1 **Table S1**: Quantum yields of water-dispersable materials emitting in the NIR-II range.

Material	QY, %	Medium	Method	Author
InAs-CdSe-ZnSe QDs	10-20	water/PBS	Integrating sphere	Bruns et al.[13]
PbS-CdS QDs	20	water	Relative to IR-26 (QY=0.5%)	Ma et al.[84]
PbS-CdS QDs	17	PBS	Integrating sphere	Tsukasaki et al.[14]
PbS-CdS QDs	5.8	water	Relative to IR-26 (QY=0.5%)	Zebibula et al.[85]
Ag_2Se QDs	29.4	n.s.	Relative to IR-26 (QY=0.5%)	Dong et al.[86]
Ag_2Se QDs	1.7	n.s.	Integrating sphere	Yarema et al.[87]
Ag_2S QDs	15.5	n.s.	Relative to IR-26 (QY=0.5%)	Zhang et al.[88]
$Na(Gd_{0.5}Lu_{0.5})F_4{:}Nd^{3+}$	25.4	dry	Integrating sphere	Mimun et al.[89]
$NaYF_4{:}Yb,Nd@CaF_2$	20.7	dry	Integrating sphere	Cao, et al.[17]
$GdF_3{:}Nd^{3+}$	10.2	dry	Integrating sphere	Pokhrel et al.[90]
$GdPO_4{:}Nd^{3+}$	9	dry	Integrating sphere	Kumar et al.[91]
$BiVO_4{:}Nd^{3+}$	1.58	dry	Integrating sphere	Starsich et al.[81]
Bioconjugate	2.6	water	Relative to IR-26 (QY=0.5%)	Zhu et al.[92]
IR-1061 in polymer	1.8	water	Relative to IR-26 (QY=0.5%)	Tao et al.[93]
Polymer particles	1.7	water	Relative to IR-26 (QY=0.5%)	Hong et al.[94]
DPP-BT dye in amphiphile	0.42	water	Relative to IR1061	Wang et al.[95]
Organic semiconductors	0.21	water	Relative to IR-26 (QY=0.5%)	Tang et al.[96]
SWCNT	0.4	water	Relative to IR-26 (QY=0.5%)	Hong et al.[97]
SWCNT	0.1	water	Relative to IR-26 (QY=0.5%)	Robinson et al.[98]
$Ba_3(V_{0.999}Mn_{0.001}O_4)_2$ (2h 800°C)	39	dry	Integrating sphere	This work
$Ba_3(V_{0.999}Mn_{0.005}O_4)_2$ (2h 600°C)	11	dry	Integrating sphere	"
$Ba_3(V_{0.999}Mn_{0.005}O_4)_2$ (2h 600°C)	4.6	water	Integrating sphere	"
BaVOMn-BiO (30min 550°C)	8.1	dry	Integrating sphere	"
BaVOMn-BiO (30min 550°C)	2.7	water	Integrating sphere	"

2 The dye IR-26 is often used as reference for relative QY measurements with a QY of 0.5 %. However,
3 more recent measurements[39] with integrating spheres determined the QY of IR-26 as 0.05 %. Therefore,
4 measurements relative to IR-26 can be up to one magnitude lower.

5 **Table S2:** Fitting parameters of fluorescence lifetime analysis fitted with a bi-exponential decay.

$$\tau = C_1 \cdot \exp\left(-\frac{t}{\tau_1}\right) + C_2 \cdot \exp\left(-\frac{t}{\tau_2}\right)$$

| Mn^{5+} concentration	τ_1 [µs]	C_1 [rel. %]	τ_2 [µs]	C_2 [rel. %]	Goodness of fit, χ^2
0.001	302.9	9.17	1020.6	90.83	0.997
0.005	207.7	15.87	673.6	84.13	1.041
0.01	152.3	26.69	487.8	73.31	1.088
0.02	100.5	35.18	341.9	64.82	1.112
0.05	46.8	46.36	218.4	53.64	1.078

6
7 **Table S3:** Size comparison of particles used in cytotoxicity and leaching experiments

Technique	$Ba_3(V_{0.995}Mn_{0.005}O_4)_2$ annealed 2 h @ 600 °C	$Ba_3(V_{0.995}Mn_{0.005}O_4)_2$ − 54.4 wt% Bi_2O_3 annealed 30 min @ 550 °C
XRD	57 nm	58 nm
BET	74 nm	56 nm
TEM	45 nm	62 nm

8

9 **SI-III: Experimental**

1 *Particle synthesis:* Particles were produced by flame spray pyrolysis.[81] Barium acetate

2 (Sigma) was dissolved at a concentration of 0.4 M in 2-ethylhexanoic acid (2-EHA, Sigma-

3 Aldrich) under magnetic stirring at 120 °C with reflux cooling for 15 h. The vanadium

4 precursor was prepared by dissolving ammonium metavanadate (Sigma-Aldrich, 99 %) at a

5 concentration of 0.4 M in a 2:1 volumetric ratio of 2-EHA to acetic anhydride (Sigma-

6 Aldrich, puriss.) under magnetic stirring at 100 °C with reflux cooling for 15 h. Liquid

7 precursors of manganese and bismuth were obtained as Mn-2-ethylhexanoate (Manganese-2-

8 ethylhexanoate, 6% Mn in mineral spirits, Alfa Aesar) and Bi-2-ethylhexanoate (Bismuth-2-

9 ethylhexanoate in 2-EHA, 92%, Alfa Aesar). These precursors were mixed stoichiometrically

10 to prepare Mn^{5+}-doped particles, where the Mn-doping concentration (x) was defined as

11 $Ba_3(V_{1-x}Mn_xO_4)_2$. For co-oxidation with Bi, the concentration (y) was defined as wt% Bi_2O_3

12 additional to 100% $Ba_3(VO_4)_2$, leading to the formula $Ba_3(V_{1-x}Mn_xO_4)_2$-y wt%Bi_2O_3. The

13 precursor mixtures were fed at 5 ml/min through a capillary and dispersed by oxygen (5

14 l/min) into fine droplets. The resulting spray was ignited and sustained by a surrounding

15 flamelet (1.5 L/min methane and 3.2 L/min oxygen). The as-prepared particles were then

16 collected on a glass microfiber filter (Whatman GF) by a gas pump (Busch Mink MM 1202

17 AV). Typical production rates using a lab-scale reactor were ~10 g/h. After synthesis,

18 particles were annealed in air for 2 h at different temperatures using heating rates of 20

19 °C/min. For annealing studies with only 30 minutes, the particles were quenched by taking

20 them out of the oven directly at the holding temperature.

21   Indocyanine green was purchased from Sigma-Aldrich. Water-soluble PbS-CdS

22 quantum dots thiol-coated terminated with a diol group were purchased from NanoOptical

23 Materials. Their core diameter is 3.1 nm and the shell thickness is 0.1 nm, as given by the

24 manufacturer.

1 *Characterization:* X-ray diffraction analysis was performed on a Bruker D8 advance

2 diffractometer operated at 40 kV and 30 mA with a step size 0.0147 °. The crystal sizes were

3 calculated using the software Topas 4.2 (Bruker) based on the Rietveld fundamental

4 parameter method. Particles were fitted using the reference patterns with ISCD = 167695 for

5 $Ba_3(VO_4)_2$ and ISCD = 62979 for Bi_2O_3. To determine the lattice parameters, the particles

6 were mixed with NiO (Sigma-Aldrich) as an internal standard for alignment. The specific

7 surface area (SSA) was measured at 77 K according to the Brunauer-Emmett-Teller (BET)

8 method (Micromeritics, Tristar II Plus), after prior degassing at 150 °C for 1 hour under

9 nitrogen. The primary particle size (d_{BET}) was calculated according to $d_{BET} = \dfrac{6}{\rho * SSA}$, where

10 the density was averaged for compositions with multiple phase by taking their mass-weighted

11 average. The transmission electron microscopy (TEM) was performed on a Tecnai F30

12 (ThermoFisher) with a field emission gun operated at 300 kV, while the scanning

13 transmission electron microscopy (STEM) combined with energy-dispersive X-ray

14 spectroscopy (EDXS) was performed on a Talos F200x microscope (ThermoFisher) with a

15 field emission gun operated at 200 kV and four attached silicon drift detectors. For electron

16 microscopy at cryo-conditions, the specimen was first coated with 1 nm carbon (BAE 120

17 thin film coating unit, Balzers, Lichtenstein) to avoid charging effects[99] and subsequently

18 mounted on a Gatan cryo-holder (Gatan Inc., Pleasanton, CA, USA) with a liquid nitrogen-

19 cooled tip. The particle size distribution was determined by manually measuring and counting

20 the longest dimensions of the particles in the obtained transmission electron images and a

21 fitted with a log-normal distribution using the OriginPro software.

22 Fluorescence measurements were typically performed in duplicates of aqueous particle

23 dispersions ($0.5\ mg_{nanoparticles}/ml + 0.5\ mg_{HSA}/ml$) after 10 minutes of ultrasonication in conical

24 polystyrene tubes (tube size: 50ml) using a water-cooled high intensity cup horn system

25 (VCX500, Sonics Vibracell, Parameters: 95 % amplitude, 28 s on, 2 s off). Fluorescence

1 spectroscopy was performed on a spectrofluorimeter system (FS5, Edinburgh Instruments)

2 equipped with a 750 nm CW laser (CNI Lasers) with 1 W (~10 W/cm^2) unless otherwise

3 specified and a xenon lamp (150 W) as excitation sources and an analogue InGaAs detector.

4 Lifetime measurements of powder samples were performed on a FLS1000 system (Edinburgh

5 Instruments) equipped with a microsecond flash lamp (60 W) and a liquid nitrogen cooled

6 NIR-PMT. The emission was fixed at 1181 nm, while excitation wavelength was between 650

7 and 750 nm, which did not affect the lifetimes. The luminescence decays were fitted with a

8 bi-exponential formula $\tau = \sum B_i * \exp^{(\frac{-t}{\tau_i})}$ using the Fluoracle software by Edinburgh

9 instruments. The intensity-weighted average lifetime was calculated using: $\langle \tau \rangle = \dfrac{\sum B_i \tau_i^2}{\sum B_i \tau_i}$ and

10 the standard deviation given by the software. Absolute quantum yield measurments of

11 powders were conducted by a Spectrofluorimeter (FS5, Edinburgh Instruments), where the

12 spectral sensitivity of detectors was accounted for. Particles were placed on a powder tray

13 within an integrating sphere (150 mm diameter) and excited using a 150 W Xenon lamp at a

14 wavelength of 750 nm. The absorption (difference between scattered light by reference and

15 sample) and emission range were scanned from 700 to 800 and 1050 to 1400 nm,

16 respectively. The QY was then calculated by the ratio of emitted to absorbed number of

17 photons, according to the formula:[100]

18
$$QY = \frac{N_{em}(\lambda_{ex})}{N_{abs}(\lambda_{ex})} = \frac{\int\limits_{1050nm}^{1400nm} I_{sample} - \int\limits_{1050nm}^{1400nm} I_{reference}}{\int\limits_{700nm}^{800nm} I_{reference} - \int\limits_{700nm}^{800nm} I_{sample}}$$

19

20 where N_{em} is the number of emitted photons, N_{abs} the number of absorbed photons, λ_{ex} the

21 excitation wavelength, and I corresponds to the intensities. As a reference, a highly scattering

22 BaSO$_4$ plug (Edinburgh Instrument) was placed inside the integrating sphere instead of the

1 powder. For QY measurements, particles were dispersed in water at 2 mg/ml using

2 ultrasonication together with HSA (2 mg/ml). The suspensions were filled into a quartz

3 cuvette and placed within the same integrating sphere and excited with a 750 nm laser. As a

4 reference material, an undoped $Ba_3(VO_4)_2$ sample also with HSA was employed with similar

5 scattering properties. Diffuse-reflectance spectra of powders were recorded in a Jasco UV-

6 VIS V-770 Spectrometer with an integrating sphere and transformed to absorption using the

7 Kubelka-Munk transformation. Fourier transformation infrared (FTIR) spectra were acquired

8 using a praying mantis accessory on a Bruker Vertex 70v. Samples were mixed with KBr at 5

9 wt% using a mortar and pure KBr acted as internal standard. Thermogravimetric analysis

10 (TGA) was performed on a TGA/DSC3+ (Mettler Toledo) under air by placing 2-10 mg of

11 powder in alumina crucibles. Selectively, the exhaust line was connected to a mass

12 spectrometer (Quadrupole MS, Pfeiffer Vacuum). For ICP-OES, 2-5 mg of powders were

13 dissolved in 3 ml nitric acid (HNO_3, 65%, Fisher Scientific) followed by the addition of 2 ml

14 of hydrogen peroxide (H_2O_2, 35%, Alfa Aesar). After ultrasonication for 10 minutes, the

15 suspensions were diluted with ultrapure water (Milli-Q, 18.2 MΩcm) and analyzed by

16 inductively coupled plasma optical emission spectroscopy (ICP-OES, Varian ICP-OES 720,

17 and Agilent 5110) using standards for calibration (Sigma-Aldrich).

18   *Centrifugation:* BaVOMn-BiO particles ($Ba_3(V_{0.995}Mn_{0.005}O_4)_2$ - 54.4wt% Bi_2O_3,

19 annealed for 30min at 550 °C) were dispersed at 2 g/L in ultrapure water (Milli-Q, 18.2

20 MΩcm) containing 2 g/L human serum albumin (HSA, Sigma-Aldrich) and ultrasonicated for

21 10 minutes with a cup-horn system. Afterwards, the suspension was kept under stirring for 1

22 hour to allow the adsorption of the HSA onto the particles. Excess HSA was removed by

23 centrifuging the suspension for 10 minutes at 10'000 rpm (11'510 RCF) and discarding the

24 supernatant. The particles were redispersed and centrifuged at increasing centrifugation

25 speeds for 10 minutes to separate several fractions. Dynamic light scattering was performed

26 on a Zetasizer (Malvern Instruments). Size distributions correspond to the average of three

1 measurements and their standard deviation. The smallest (5 – 7.8 krpm) and largest size

2 fractions (0 – 0.5 krpm) have been analyzed with electron microscopy and size distributions

3 have been extracted using NanoDefine Particle Sizer Software, according to a standardized

4 protocol.[101]

5 *Stability testing:* A stock solution of BaVOMn-BiO ($Ba_3(V_{0.995}Mn_{0.005}O_4)_2$ - 54.4wt% Bi_2O_3,

6 annealed for 30 min at 550 °C) was prepared at 5 mg/ml in water together with the same mass

7 of HSA, and dispersed for 10 minutes in the above mentioned ultrasonication device. Then,

8 the stock solution was mixed with the final medium (water, NaCl 0.154M, PBS, RPMI cell

9 medium) at a volume ratio of 1:9 in triplicates and vortexed. The suspensions were kept under

10 constant stirring during the testing period and characterized at the given time intervals. For the

11 leaching tests, the suspensions were centrifuged for 30 minutes (10'000g) after 14 days to

12 separate the dissolved ions from the remaining nanoparticles. The supernatant was then taken

13 and diluted in 5 % HNO_3 for ICP-OES analysis. 100 % of the nominal dose corresponds to

14 particles fully dissolved by 5 % HNO_3 and analyzed by ICP-OES. The same protocol was

15 applied for BaVOMn ($Ba_3(V_{0.995}Mn_{0.005}O_4)_2$ annealed 2h at 600 °C). For the chemical

16 stability, the stock solution was mixed with a ratio of 1:9 with aqueous solutions, where the

17 pH has been adjusted to 2-11 using NaOH and HCl.

18 *In vitro and ex vivo experiments:* Human cervical carcinoma (HeLa) cells (ATCC CCL-2)

19 were cultured in Minimum Essential Medium (MEM) containing 10 % fetal calf serum (FCS),

20 1 % non-essential amino acids (NEAA), 1% L-Glutamine, 1% penicillin-streptomycin-

21 neomycin (PSN) and 1 mM sodium pyruvate, at 37 °C in a humidified atmosphere containing

22 5 % CO_2. The cells were sub-cultured every fourth day and grown to 75 % confluence.

23 For cytotoxicity experiments, 10 000 Hela cells were seeded in a sterile black 96 well plate in

24 a full cell culture medium and left to attach overnight. Then, freshly prepared BaVOMn and

25 BaVOMn-BiO suspensions at the desired concentration, QD suspensions, $BaCl_2$ and

1   Na$_3$VO$_4$, or vehicle controls were added (100 µl) to the wells resulting in a final particle

2   concentration ranging from 0 up to 1000 µg mL^{-1} and were incubated for 24 h at 37 °C under

3   humidified atmosphere containing 5 % CO$_2$. ddH$_2$O was used as a negative control and Triton

4   X-100 (1 % solution) as a positive control. The total ddH$_2$O content was kept 10 % in each

5   well. After the incubation, the supernatant was discarded and 50 µl of fresh full cell culture

6   medium was mixed with equal amount of the substrate mix from Promega CellTiter-Glo® 3D

7   Cell Viability Assay kit. The plates were incubated on the shaker in the dark for 30 minutes at

8   room temperature and luminescence was measured using a Mithras LB 943 Multimode Plate

9   Reader.

10   For fluorescence microscopy experiments, Hela cells were seeded on ibidi Gridded

11   Glass Coverslips Grid-50 at density of 12'700 cells/cm^2 in full cell culture medium and left to

12   attach for 24 h. Next, cells were incubated with BaVOMn-BiO nanoparticles (500 µg for 100

13   000 cells) for 24 h in fresh full cell culture medium. Then, cells were gently washed with pre-

14   warmed sterile PBS and fixed with 4 % methanol-free paraformaldehyde (PFA) and 0.1 %

15   Triton X-100 (Sigma-Aldrich, T8787) solution for 1 hour. This fixation was required to

16   correlate images taken with different fluorescence microscopes (one for the visible region,

17   one for NIR-II), as detailed below. After the fixation, cells were thoroughly washed 3 times

18   for 5 minutes each with PBS, the cytoskeleton was stained with Alexa 488 Phalloidin

19   (Invitrogen, A12379, staining solution: 10 µL stock to 1 ml ddH$_2$O) and the nuclei were

20   stained with DAPI (Sigma Aldrich, D9542, staining solution: 1 µL stock to 1 ml ddH$_2$O).

21   After 1 h incubation, the cells were washed 5 times with ddH$_2$O for 5 minutes and kept in

22   ddH$_2$O until imaging. Fluorescence images of DAPI and Alexa 488 Phalloidin were acquired

23   with Carl Zeiss Axio Imager M1 using Blue (excitation 359 ± 24 nm, emission 445 ± 25 nm,

24   exposure time 40 ms) and Green (excitation 455 ± 20 nm, emission 530 ± 25 nm, exposure

25   time 500 ms) filter cubes, respectively. For NIR imaging, a 750 nm continuous wave laser

26   was used to illuminate the sample on an inverted Nikon microscope. The collimated laser

1 beam was defocused with an achromatic lens (AC254-400-A-ML, Thorlabs), deflected at a

2 50/50 beamsplitter and directed into an objective (50x/NA0.80 TU Plan Fluor, Nikon). The

3 beam spot diameter on the sample was approximately 190 μm, and the power at the sample

4 plane 14.0 μW (0.05 W/cm^2). The same objective was used to collect the emitted light. The

5 emitted light was passed through a 50/50 beamsplitter and a 900 nm longpass filter to

6 eliminate reflections of the excitation beam in the emission path. Images were taken with an

7 InGaAs camera (Ninox, Raptor Photonics) cooled to -15°C. The integration time was set to

8 200 ms and the high gain acquisition mode was used. Additionally, bright-field images were

9 recorded on the same setup. To overlay the images obtained by the two setups, the images

10 were aligned and scaled using the grids on the microscopy slide.

11   For *ex vivo* experiments, BaVOMn-BiO particles annealed for 30 min at 550 °C were

12 dispersed in water at 5 mg/ml using ultrasonication and mixed 1:1 with a hot 1 wt% agar-

13 containing water solution and inserted into 2 glass capillaries (diameter = 1.5 mm), where the

14 mixture cooled off and solidified. Similarly, PbS-CdS QDs and ICG were mixed with agar

15 and filled into capillaries with a final concentration of 1 and 0.01 mg/ml,[102] respectively. The

16 capillaries were covered with pieces of chicken breast tissue of varying thickness (0 – 10 mm)

17 and illuminated with a 750 nm laser (CNI). The fiber-coupled laser (1.44 W) was spectrally

18 filtered with a 750 nm bandpass (Thorlabs) and enlarged using a collimator (CNI) and a

19 diffusor (Thorlabs) to an area of 7 cm in diameter, resulting in power densities of 0.0374

20 W/cm^2. The fluorescent signal was collected using the same InGaAs camera (cooled to -15

21 °C) and a SWIR lens (Fuchsia, 25 mm, F1.4 SWIR lens) equipped with two 850 nm long-pass

22 filter (Thorlabs, FELH850) to remove any signal from the laser. The analog gain of the

23 camera was set to high, and the exposure time was adjusted (range: 0.4 to 30 ms) to reach a

24 maximum signal intensity close to saturation. The FWHM was evaluated by taking three

25 intensity profiles per capillary perpendicular to the long axis and fitting it with a Gaussian

26 profile using the OriginPro Software. The signal to background ratio was evaluated by

1 dividing the average of the 100 brightest pixel by the average of a control experiment without

2 any fluorescent agent on chicken tissue with laser irradiation and the same exposure time. The

3 results are given as the average and standard deviation of these values.

4

5 **SUPPORTING REFERENCES**

6 66. R. D. Shannon, *Acta Crystallogr. A*, 1976, **32**, 751-767.

7 67. S. Laha, S. Tamilarasan, S. Natarajan and J. Gopalakrishnan, *Inorg. Chem.*, 2016, **55**,
8 3508-3514.

9 68. P. Jiang, J. Li, A. Ozarowski, A. W. Sleight and M. A. Subramanian, *Inorg. Chem.*,
10 2013, **52**, 1349-1357.

11 69. K. Dardenne, D. Vivien and D. Huguenin, *J. Solid State Chem.*, 1999, **146**, 464-472.

12 70. O. Svelto, *Springer Handbook of Lasers and Optics*, Springer, New York City, 2012.

13 71. X. W. Zhang, J. M. Nie, S. S. Liu and J. R. Qiu, *J. Mater. Sci.-Mater. El.*, 2018, **29**,
14 6419-6427.

15 72. P. Tarte and J. Thelen, *Spectrochim. Acta a-M.*, 1972, **A 28**, 5-14.

16 73. E. J. Baran and S. G. Manca, *Spectrosc. Lett.*, 2006, **15**, 455-462.

17 74. X. W. Zhang, Y. Li, Z. L. Hu, Z. Chen and J. R. Qiu, *RSC Adv.*, 2017, **7**, 10564-
18 10569.

19 75. R. P. Cao, X. G. Yu, X. Y. Sun, C. Y. Cao and J. R. Qiu, *Spectrochim. Acta A*, 2014,
20 **128**, 671-673.

21 76. D. Dexter and J. H. Schulman, *J. Chem. Phys.*, 1954, **22**, 1063-1070.

22 77. U. Oetliker, M. Herren, H. U. Gudel, U. Kesper, C. Albrecht and D. Reinen, *J. Chem.*
23 *Phys.*, 1994, **100**, 8656-8665.

24 78. H. R. Verdun, *OSA Proc.*, 1993, **15**, 315-319.

25 79. B. del Rosal, D. H. Ortgies, N. Fernandez, F. Sanz-da, D. Jaque and E. M. Rodriguez,
26 *Adv. Mater.*, 2016, **28**, 10188-10193.

27 80. D. H. Ortgies, M. L. Tan, E. C. Ximendes, B. del Rosal, J. Hu, L. Xu, X. D. Wang, E.
28 M. Rodriguez, C. Jacinto, N. Fernandez, G. Y. Chen and D. Jaque, *ACS Nano*, 2018,
29 **12**, 4362-4368.

30 81. F. H. L. Starsich, P. Gschwend, A. Sergeyev, R. Grange and S. E. Pratsinis, *Chem.*
31 *Mater.*, 2017, **29**, 8158-8166.

32 82. L. Madler and S. E. Pratsinis, *J. Am. Ceram. Soc.*, 2002, **85**, 1713-1718.

33 83. R. Marin, A. Skripka, L. V. Besteiro, A. Benayas, Z. Wang, A. O. Govorov, P. Canton
34 and F. Vetrone, *Small*, 2018, **14**.

35 84. Z. R. Ma, M. X. Zhang, J. Y. Yue, C. Alcazar, Y. T. Zhong, T. C. Doyle, H. J. Dai and
36 N. F. Huang, *Adv. Funct. Mater.*, 2018, **28**, 1803417.

37 85. A. Zebibula, N. Alifu, L. Q. Xia, C. W. Sun, X. M. Yu, D. W. Xue, L. W. Liu, G. H.
38 Li and J. Qian, *Adv. Funct. Mater.*, 2018, **28**, 1703451.

39 86. B. H. Dong, C. Y. Li, G. C. Chen, Y. J. Zhang, Y. Zhang, M. J. Deng and Q. B. Wang,
40 *Chem. Mater.*, 2013, **25**, 2503-2509.

41 87. M. Yarema, S. Pichler, M. Sytnyk, R. Seyrkammer, R. T. Lechner, G. Fritz-Popovski,
42 D. Jarzab, K. Szendrei, R. Resel, O. Korovyanko, M. A. Loi, O. Paris, G. Hesser and
43 W. Heiss, *ACS Nano*, 2011, **5**, 3758-3765.

44 88. Y. Zhang, G. S. Hong, Y. J. Zhang, G. C. Chen, F. Li, H. J. Dai and Q. B. Wang, *ACS*
45 *Nano*, 2012, **6**, 3695-3702.

89. L. C. Mimun, G. Ajithkumar, C. Rightsell, B. W. Langloss, M. J. Therien and D. K. Sardar, *J. Alloy. Compd.*, 2017, **695**, 280-285.

90. M. Pokhrel, L. C. Mimun, B. Yust, G. A. Kumar, A. Dhanale, L. Tang and D. K. Sardar, *Nanoscale*, 2014, **6**, 1667-1674.

91. G. A. Kumar, N. R. Balli, M. Kailasnath, L. C. Mimun, C. Dannangoda, K. S. Martirosyan, C. Santhosh and D. K. Sardar, *J. Alloy Compd.*, 2016, **672**, 668-673.

92. S. J. Zhu, S. Herraiz, J. Y. Yue, M. X. Zhang, H. Wan, Q. L. Yang, Z. R. Ma, Y. Wang, J. H. He, A. L. Antaris, Y. T. Zhong, S. Diao, Y. Feng, Y. Zhou, K. A. Yu, G. S. Hong, Y. Y. Liang, A. J. Hsueh and H. J. Dai, *Adv. Mater.*, 2018, **30**, 1705799.

93. Z. M. Tao, G. S. Hong, C. Shinji, C. X. Chen, S. Diao, A. L. Antaris, B. Zhang, Y. P. Zou and H. J. Dai, *Angew. Chem. Int. Edit.*, 2013, **52**, 13002-13006.

94. G. S. Hong, Y. P. Zou, A. L. Antaris, S. Diao, D. Wu, K. Cheng, X. D. Zhang, C. X. Chen, B. Liu, Y. H. He, J. Z. Wu, J. Yuan, B. Zhang, Z. M. Tao, C. Fukunaga and H. J. Dai, *Nat. Commun.*, 2014, **5**, 4206.

95. Q. Wang, Y. N. Dai, J. Z. Xu, J. Cai, X. R. Niu, L. Zhang, R. F. Chen, Q. M. Shen, W. Huang and Q. L. Fan, *Adv. Funct. Mater.*, 2019, **29**, 1901480.

96. Y. F. Tang, Y. Y. Li, X. M. Lu, X. M. Hu, H. Zhao, W. B. Hu, F. Lu, Q. L. Fan and W. Huang, *Adv. Funct. Mater.*, 2019, **29**, 1807376.

97. G. S. Hong, S. Diao, J. L. Chang, A. L. Antaris, C. X. Chen, B. Zhang, S. Zhao, D. N. Atochin, P. L. Huang, K. I. Andreasson, C. J. Kuo and H. J. Dai, *Nat Photonics*, 2014, **8**, 723-730.

98. J. T. Robinson, G. S. Hong, Y. Y. Liang, B. Zhang, O. K. Yaghi and H. J. Dai, *J. Am. Chem. Soc.*, 2012, **134**, 10664-10669.

99. Q. Chen, C. Dwyer, G. Sheng, C. Zhu, X. Li, C. Zheng and Y. Zhu, *Adv. Mater.*, 2020, **32**.

100. C. Wurth, M. Grabolle, J. Pauli, M. Spieles and U. Resch-Genger, *Anal. Chem.*, 2011, **83**, 3431-3439.

101. E. Verleysen, T. Wagner, H.-G. Lipinski, R. Kägi, R. Koeber, A. Boix-Sanfeliu, P.-J. De Temmerman and J. Mast, *Materials*, 2019, **12**, 2274.

102. R. Benson and H. Kues, *Phys. Med. Biol.*, 1978, **23**, 159-163.